Heat Transfer and Combustion Characteristics of Nano-Sized Aluminum and Aluminum Oxide Utilizing Advanced Laser and Optical Diagnostics

A THESIS

SUBMITTED TO THE FACULTY OF THE GRADUATE SCHOOL OF THE

UNIVERSITY OF MINNESOTA

BY

Hayoung Jeong

IN PARTIAL FULFILLMENT OF THE REQUIREMENTS

FOR THE DEGREE OF MASTER OF SCIENCE

Dr. Sayan Biswas

January 2024

Acknowledgments

My journey was made possible through the generous help and support of many individuals. Foremost among them is Dr. Sayan Biswas, my advisor, whose invaluable support and guidance not only molded my academic journey but also played a pivotal role in shaping my life. Dr. Biswas, with endless patience, waited for my steps and became a guiding light, making it possible for me to reach this point. I extend my appreciation to Dr. William Northrop and Dr. Victor Barocas for willingly serving as committee members and sparing their time for valuable feedback. Dr. Dilip Sundaram from the Indian Institute of Technology Gandhinagar played a crucial role in the early stages of my research, offering valuable advice and guidance through numerous meetings.

The 3P Lab provided a vibrant and supportive environment, and I am grateful for the help and inspiration received from my wonderful colleagues. In particular, having Binit as my mentor was a stroke of luck. The endless assistance and advice he provided will be cherished throughout my life. Oluwasegun's warm encouragement and willingness to help were also deeply appreciated.

Special thanks to Cindy, my ever-reliable friend, and KC, Eunice, James, and Mirae, the additional family I found in Minnesota during my time away from home. I express my thanks for the love and encouragement provided by Pastor Kim and Mrs. Kim.

Dedication

To my family, who has supported and shaped the person I am today with unconditional love and unwavering support—my respected parents, dear father and mother, and my beloved, one and only brother, Woohyun.

Abstract

The present study uses advanced optical diagnostics to explore the heat transfer and combustion characteristics of nano-sized aluminum and alumina (aluminum oxide) particles. The study employs a two-prong approach, conducting two distinct experiments utilizing nano-aluminum and nano-alumina. Alumina forms an oxide coating on aluminum, requiring an understanding of the associated heat transfer characteristics. The first part of this study focuses on determining the accommodation coefficient of nano-alumina particles. The accommodation coefficient represents the efficiency of a gas in removing heat from a surface, expressed as the ratio of the actual heat loss to the ideal loss. A comprehensive mathematical framework has been developed for calculating the accommodation coefficient utilizing a two-colored time-resolved Laser-Induced Incandescence technique (TiRe-LII). The model's validity was confirmed by comparing it with data from existing literature. This model serves as a reliable foundation for measuring the accommodation coefficient in future studies involving particles other than alumina. The second part of the study utilizes Laser-induced Air Shock from Energetic Material (LASEM) to assess the energetic behavior of nano-aluminum. LASEM is employed to measure and compare the shockwave velocity generated by laser-induced combustion of both nano-aluminum and nano-alumina particles. The observed shockwave velocity from aluminum surpasses that from alumina, indicating higher energy content in aluminum. LASEM proves to be an effective lab-scale technique, capable of characterizing energetic behavior with minimal sample material (~ milligram). Intermediate species (e.g., AlO, Al, O, etc.) emissions from laser-induced plasma and combustion signals affirm exothermic reactions in the early

stages, supporting the hypothesis that these reactions contribute to the increased shockwave velocity of aluminum particles. These findings significantly enhance our understanding of nanoparticle combustion phenomena.

Table of Contents

List of Figures

List of Tables

List of Abbreviations

List of Symbols, Abbreviations, and Acronyms	
Nomenclature	
Al	aluminum
AlO	aluminum monoxide
Al_2O_3	alumina
Ar	argon
CO_2	carbon dioxide
c	speed of light
c_g	gas velocity
c_p	Specific heat of gas
d_p	particle diameter
E	spectral emission
He	helium
h	Plank's constant
K_n	Knudsen number
k_B	Boltzmann constant
m	mass
p	pressure
N_2	nitrogen
N_A	Avogadro's number
q_{cond}	conduction heat flux
q_{evap}	evaporation heat flux
q_{rad}	radiation heat flux
R	gas constant
R_{BB}	blackbody energy spectral density
T	temperature
t	time
Greek	
α	accommodation coefficient
γ	specific heat ratio
ε	emissivity
Λ	mean free path
λ	wavelength
τ	optical parameter
Subscripts and Superscripts	
a	ambient gas
g	gas
L	lamp
p	particle

Chapter 1: Introduction and Overview

1.1 Introduction

The combustion of metal fuel particles, particularly aluminum, has been a subject of research for several decades and continues to be an active area of research for the development of new energy sources and propulsion systems [1]. Aluminum has significant reserves and can be considered a sustainable alternative energy source as opposed to hydrocarbon-based fuels, which are non-renewable and have the potential for fuel depletion [2]. Aluminum is also environmentally friendly, as its combustion products are non-toxic and non-polluting. Beyond Earth, recent missions to the moon have discovered deposits of Aluminum and Titanium near the lunar south pole, indicating potential resources for future propellant production. Furthermore, aluminum's high energy density (Aluminum has an energy density of 80 kJ/cm³, while liquid jet fuel JP-10 has an energy density ranging from 35 to 40 kJ/cm³) makes it an excellent candidate for use in explosives and propellants. By understanding the combustion mechanism of aluminum particles, researchers can optimize its use as a primary fuel in various applications, including space and underwater propulsion, combustion, battery, solar cell, catalysis, pyrotechnic, hydrogen generation, explosives, and propellants [3]–[5].

However, several problems have limited the use of aluminum as the primary 'standalone' fuel. Aluminum has a high affinity for oxygen and readily reacts with it to form an inert layer of oxide on its surface known as alumina (Al_2O_3). This alumina layer acts as a protective barrier, preventing additional oxidation and combustion of aluminum particles [6]. The alumina layer is undesirable due to its inert nature, poor heat conductivity,

and adverse impact on total volumetric energy density. Additionally, the stable alumina layer is challenging to remove and requires high temperatures for breakdown, resulting in increased energy loss during aluminum combustion. However, The use of nano-sized particles offers a promising avenue for enhancing the combustion characteristics. Particle size determines the combustion timescale for metal particles [7]. When the particles are large (micron-sized particles), the combustion time is longer, and the particles are not completely burned in the combustion chamber (e.g., solid rocket thruster), which may cause a decrease in combustion efficiency. Nano-sized aluminum particles have a much higher surface-area-to-volume ratio than micro-sized particles, enabling faster reaction rates and facilitating easier ignition than larger aluminum particles. As the particle diameter decreases from the micro to the nanoscale, a decrease in the ignition temperature and melting temperature of the particles has been observed, as depicted in **Figure 1**.

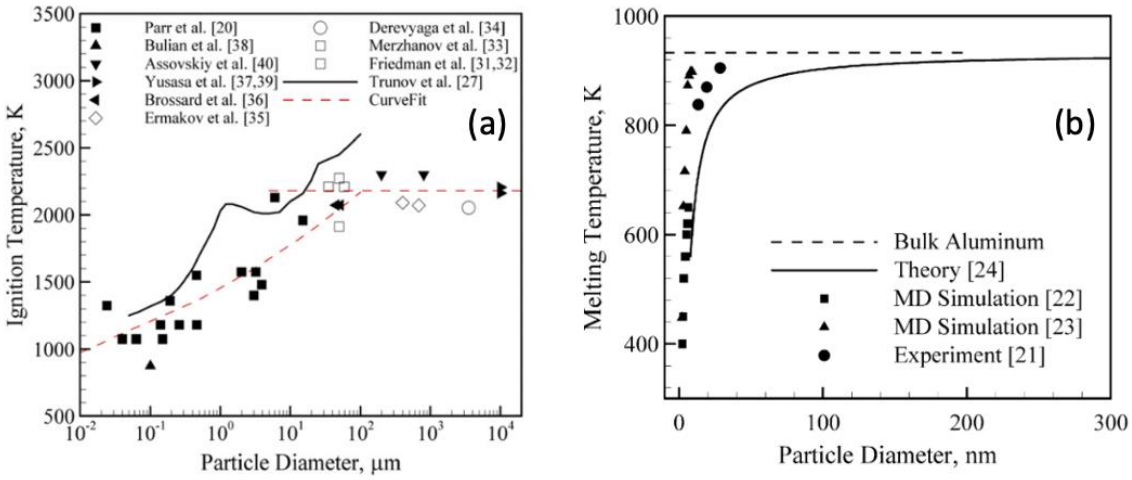

Figure 1 *(a) Aluminum melting temperature as a function of particle diameter. (b) Ignition temperature of aluminum particles as a function of particle diameter in oxygen-containing environments* [7].

Recent developments in innovative particle manufacturing techniques have offered some degree of control over oxide layer thickness and improved management of combustion

efficiency [8]. Nevertheless, the issue has not been completely eradicated. To effectively use aluminum particles for energy applications, it is crucial to characterize both nano-aluminum and nano-alumina particles and understand their heat transfer and combustion characteristics.

1.1.1 Accommodation coefficient of nano aluminum oxide particles

The combustion process of aluminum particles can be segmented into three stages, characterized by phase transformations and chemical reactions. **Figure 2** illustrates the progression of oxidation in nano-aluminum particles. In the first stage of aluminum combustion, the particle's core is heated until it reaches the melting temperature. Aluminum melts at approximately 660 degrees Celsius (1220 degrees Fahrenheit), while aluminum oxide has a much higher melting point at around 2,070 degrees Celsius (3,760 degrees Fahrenheit). Due to the mismatch in melting temperatures, the solid aluminum core undergoes a phase transition to the liquid/molten phase in the second stage. During this stage, energy and mass transfer occur from the hot gas surrounding the particle through the Al_2O_3 oxide layer to the aluminum core. However, until the oxidizer comes in contact with the aluminum core, the combustion cannot take place. In the third and final stage, the expansion of the molten aluminum core ruptures the aluminum oxide layer (note the oxide has a poor expansion coefficient), and then only the oxidizer comes in contact with the molten aluminum. This starts the aluminum combustion process. Hence, understanding the combustion mechanism of aluminum particles begins with a clear understanding of the heat transfer mechanism of aluminum oxide/alumina.

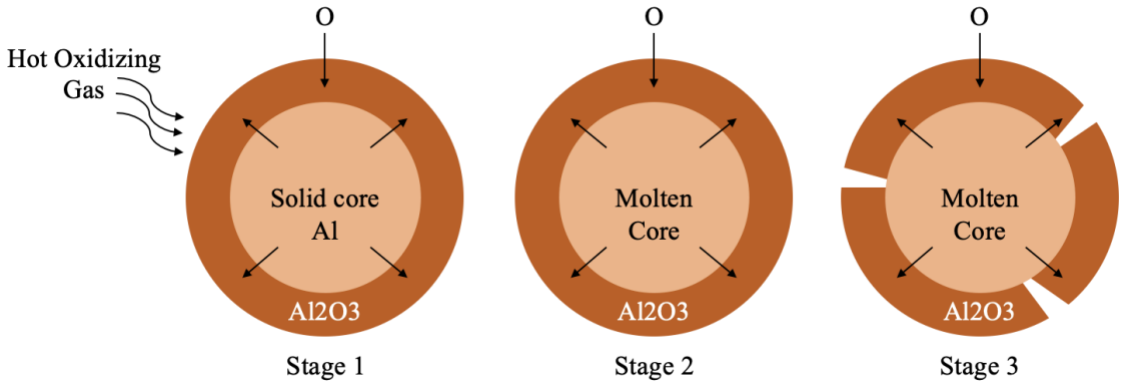

Figure 2 *Three stages of oxidation of nano aluminum particles.*

When the particle diameter is much smaller than the mean free path, i.e., when heat conduction can occur within the free molecular regime (characteristics of nano-sized particles), heat conduction is governed by a relatively simple equation. During Stage 1 and Stage 2 (prior to the rupture of the oxide layer), mass diffusion of aluminum takes place through electron tunneling [9]. Electron tunneling is the quantum phenomenon where electrons can pass through potential energy barriers. Aluminum valence electrons move to the surface of the oxide layer through tunneling [10], [11]. These electrons ionize the absorbed oxygen within the oxide layer, creating an electric field that reduces the energy barrier for the diffusion of oxygen molecules. Consequently, heat transfer from the hot gasses and exothermic reactions with diffused oxygen molecules result in the melting of the core in the initial combustion stage.

The physics of heat transfer at the nanoscale is intriguing, and nanoparticle combustion differs significantly from traditional gas-phase combustion in CHON systems. For example, CHON systems (e.g., fuel-rich hydrocarbon combustion) produce soot particles during combustion; soot particles are primarily in a transition regime where the particle diameter is comparable to the mean free path of the gas molecules [12]. In this case,

the Boltzmann equation, which governs heat conduction, becomes particularly challenging to solve analytically because the particles can interact with gas molecules through various mechanisms, including collisional transfer of energy and chemical reactions [12]. Liu et al. showed that the Fuchs model (Equation 1.2) is applicable to the full range of Knudsen numbers (Equation 1.1) from the free molecule regime to the continuum regime. In other words, the transition regime heat transfer from a single nano-sized particle can be accurately modeled using the Fuchs model [13].

$$K_n = \frac{2\Lambda}{d_p} \tag{1.1}$$

$$q_{cond} = \pi {d_p}^2 \frac{\alpha p_g c_g}{8T_a} \frac{\gamma+1}{\gamma-1} \left(T_p - T_a\right) \tag{1.2}$$

In **Equation 1.2**, $\boldsymbol{\alpha}$ stands for the particle accommodation coefficient and is a fundamental parameter that characterizes the efficiency of heat transfer between gas molecules and the surface of a particle during a collision [14]. Therefore, having precise knowledge of the accommodation coefficient of nano-alumina plays a pivotal role in understanding the combustion mechanism of nano-aluminum particles.

Time-**Re**solved **L**aser-**I**nduced **I**ncandescence (TiRe-LII) stands out as the most precise experimental technique for determining the particle accommodation coefficient in well-characterized particle samples with known size distributions [15]. LII is a powerful tool in combustion diagnostics that has been extensively used to measure the soot volume fraction and primary particle size in various applications [16]. LII technique uses laser light to heat up particles to the point where they are incandescent or glow. The resulting light emission is then measured and analyzed to provide information about the particles.

The present study has developed a comprehensive framework for measuring the accommodation coefficient of alumina particles using time-resolved experimental data. A novel experimental arrangement was built to **calculate accommodation coefficients precisely**. Unfortunately, the extended lead time for the custom photomultiplier (PMT) tube prevented timely experimentation. Instead, literature data was employed to validate the developed methodology. Nonetheless, the developed framework will make valuable contributions to future nanoscale heat transfer research.

1.1.2 Combustion of nano aluminum particles

As illustrated in **Figure 2**, in the first stage, the aluminum core reaches its melting temperature due to heat exchange between the gas and particle surfaces within the oxide layer, along with mass and energy diffusion within the particle. Sundaram et al. provided a detailed explanation of the combustion stages of aluminum in his paper [17].

The second stage commences with the melting of the aluminum core, leading to pressure buildup and facilitating the outward movement of molten aluminum through diffusion and/or flow within cracks in the oxide layer. After melting, polymorphic phase transformations occur, creating openings in the oxide layer. The molten aluminum reacts with the oxidizing gas, resulting in the release of energy and the ignition of nano-aluminum particles. Due to the lower density of liquid aluminum ($2.37\ \mathrm{g/cm^3}$) compared to its solid phase density ($2.54\ \mathrm{g/cm^3}$), volumetric expansion occurs, resulting in compressive stress on the core and tensile stress on the shell induced. This leads to the cracking of the oxide layer and the subsequent ignition of the aluminum core. The ignition delay, an inherent material characteristic determining the time required for ignition, depends on factors such as heating rate, particle size, oxidizing gas composition, and pressure. Fabien et al.

conducted experiments with a single 88 μm aluminum particle suspended in air, revealing an ignition delay of 3 milliseconds when ignited by a CO_2 laser with a power of 50 W and a wavelength of 10.6 μm. In comparison to Fabien's micron-sized single-particle combustion, nano-sized particles are anticipated to exhibit shorter ignition delays [18].

In the final phase of combustion, aluminum vigorously reacts with oxygen, resulting in the formation of aluminum oxide. These reactions encompass both surface combustion in the liquid phase and vapor phase combustion. Sundaram et al. discovered that the adiabatic flame temperature of aluminum is lower than its boiling temperature when subjected to pressures exceeding 100 atm in the air, as determined by the NASA Chemical Equilibrium Analysis (CEA) code [17]. This indicates that surface reactions are dominant in pressure regimes exceeding 100 atm, which is highly relevant for solid rocket combustors [19].

Laser-Induced Air Shock from Energetic Material (LASEM) has been a key focus in the research of material characterization involving the interaction of focused lasers with various materials. When a high-energy pulse laser is directed at a material, it leads to material ablation, plasma formation, and the generation of a shock wave due to gas expansion. In the case of energetic materials such as aluminum, boron, titanium, etc., the ablated material undergoes exothermic reactions, influencing the speed of the shock wave. The Army Research Laboratory (ARL) has utilized the LASEM technique to analyze explosives (such as TNT, CL-20, RDX) in a laboratory-scale setting using minimal amounts of explosives (milligrams to grams). This approach correlates the performance with kilogram amounts of explosives by comparing the LASEM shock speed to the actual detonation velocity [20]. Although LASEM has been used to characterize explosives, its

application for propellants and energetic metals like aluminum has been limited. In this study, LASEM experiments on aluminum particles were conducted to investigate the correlation between shockwave velocity and exothermic reactions. This study aims to investigate the appropriate laser power density for examining the LASEM exothermic reaction of nano-aluminum particles. Additionally, it provides insights into the correlation between exothermic reactions and radical and intermediate species formation.

1.2 Review of Key Relevant Literature

Altman et al. [14] conducted experimental estimations to determine the accommodation coefficient of silica nanoparticles situated within a combustion zone at a high temperature of 2000K. The conventional approach for determining the accommodation coefficient involves measuring the temperature ratio of a solid body and surrounding gas for a known incident heat flux. A critical assumption in accommodation coefficient measurement is that the incident laser exclusively heats the particles, not the surrounding gas. To address concerns about potential gas heating due to laser irradiation absorption, Altman conducted a dedicated experiment measuring gas temperature in a flame exposed to a laser without nanoparticles. At 1000 W laser power, the combustion gas temperature increase stayed below 100 K, suggesting a potential accommodation coefficient error of no more than 15%. Another critical assumption is that the particles do not contribute to the gas heating. Dismissing gas heating from silica nanoparticles due to their small volume fraction in the flame, Altman stated that if heat transfer between irradiated particles and gas is insignificant, the change in particle temperature is proportional to the particle volume fraction. To confirm minimal gas heating, they experimentally measured particle

temperature variation in different flame regions, determining relative particle volume fractions through scattering measurements. The results indicated minimal dependence of particle temperature change on particle volume fraction. Altman's research unveiled a remarkably low upper limit (~ 0.005) for the accommodation coefficient of silica nanoparticles. They suggested that the substantial decrease in the accommodation coefficient at high temperatures, contrary to the commonly used value of unity, indicates inefficient heat transfer between gas and particles in conditions of gas-particle collisions in the free-molecular regime.

A key contribution to the measurement of the accommodation coefficient was carried out by Allen et al. [15], and this work will be discussed in detail. It holds significant importance in understanding the relevance and significance of the current study. Allen performed time-resolved laser-induced incandescent (TiRe-LII) measurements to measure the accommodation coefficient of nano-alumina particles in helium, nitrogen, and argon. Allen rapidly heated the nano alumina particles using the fundamental 1064 nm wavelength Quantel Brilliant Nd: YAG laser and monitored the incandescence of the nanoparticles using a two-color TiRe-LII setup. The two-color TiRe-LII setup consisted of an f/2 collection lens focusing the particle incandescence onto a bifurcated fiber optic. Light from each path passed through a bandpass filter of 705 nm and 826 nm wavelengths and was collected in a photomultiplier tube. The signals from the photomultiplier tubes were amplified using a Stanford Research Systems Quad preamplifier with a 300 MHz bandwidth and collected using a Lecroy 9360 300 MHz oscilloscope. The experiments were conducted in a chamber filled with helium, nitrogen, or argon at varying pressures, focusing on 2 atm pressure with a Knudsen number of ~2. Approximately 20 mg of

particles were injected, and the laser pulse parameters were set at 5 ns duration and 20 Hz repetition rate. The LII signal was averaged over 15 laser pulses, and the system was calibrated using a tungsten lamp. The aluminum oxide particles used in the study were sourced from Alfa Aesar, with a nominal size of 40–50 nm and 99.5% purity. Unlike previous LII efforts focused on synthesizing particles, Allen's study involved pre-made particles injected into the experimental chamber. Particle size distribution was directly measured using scanning electron microscopy (SEM), analyzing over 300 particles to ensure a statistically significant sample. The results revealed significant size variation, depicted in a histogram and a representative SEM image (**Figure 3**), highlighting the spherical nature of the particles with minimal agglomeration. The SEM analysis utilized a Hitachi S4700 instrument.

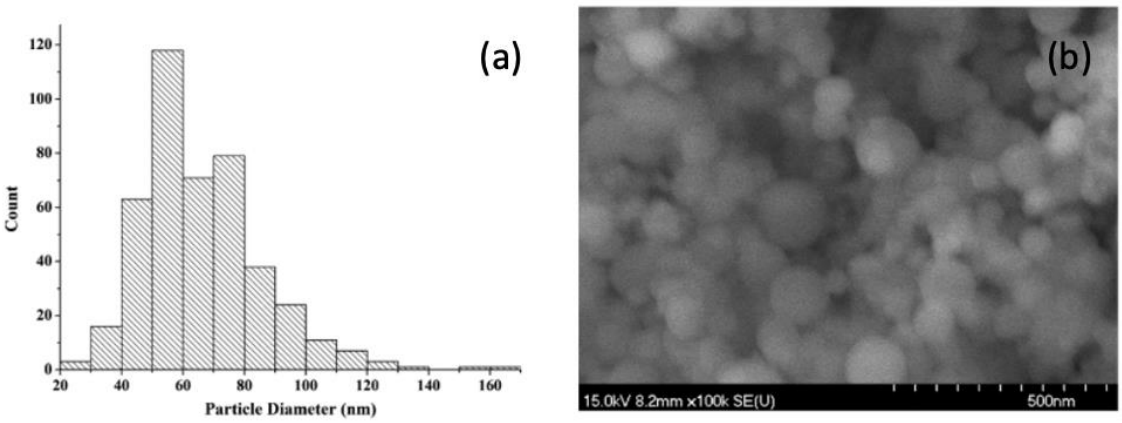

Figure 3 *(a) Histogram of the nano-alumina particle size from the measured SEM analysis. (b) SEM image of the nanoparticles using a Hita-measured SEM analysis* [15].

In different gaseous environments, accommodation coefficients were 0.03, 0.07, and 0.15 in helium, nitrogen, and argon at 300 K and 2 atmospheres, respectively. Allen compared incandescent signals with and without particle injection. When particles were absent, the observed signal was significantly lower (but not zero) compared to the case

with particles, indicating that the emission is likely due to particle incandescence. They speculated that the observed signal without particles can also arise from other laser-induced emission (LIE) processes, such as emission from species vaporized from heated nanoparticles, chemiluminescence from recombining vaporized products, and particle plasmon resonance. However, each process typically occurs at very fast rates (~ femto- to sub-micro second), while particle incandescence is a longer-lived process (~ millisecond). In the free-molecular regime of heat conduction, there is a clear ambient pressure dependence on the heat transfer rate, and in the continuum regime, heat transfer is expressed by Newton's law of cooling. In the continuum regime, the Nusselt number for spherical particles is independent of pressure. The thermal conductivity is relatively insensitive to pressure until very low pressures (~100 Pa) are reached. This suggests that particle heat transfer in the continuum regime is expected to be pressure-independent. Allen demonstrated this by linearly fitting the logarithm of the temperature particle/ambient temperature difference to pressure-dependent data at 1.06 and 2.08 atm in helium. The pressure dependence of the LII signal indicates that the observed LII is primarily due to primary nanoparticles and not compacted clusters of agglomerated primary particles. To properly weigh temperature profiles for each individual particle size within the distribution, they modeled temperature profiles for each size bin using a specified accommodation coefficient. Then, the curves were averaged. Once the transient temperature profile for each particle size bin was calculated, the temperature was converted to a transient intensity profile using Planck's law. The resulting effective temperature distribution, after proper weighting, was then compared to the measured temperature. Allen provided an example of modeled temperature for various particle sizes and the resulting effective temperature

distribution. Using the optimal accommodation coefficients, Allen presented fitted experimental temperature measurements for three conditions: nitrogen (N2) at 300K and 2 atm, argon (Ar) at 300K and 2 atm, and helium (He) at 300K and 2 atm. To eliminate experimental errors caused by various LIE processes mentioned earlier, Allen excluded the first 100 ns from the fitting procedure. Allen presented the fitting results and uncertainty range of the accommodation coefficient in **Table 1**. Eremin et al. [21] found an accommodation coefficient of 0.01 for iron nanoparticles in helium and 0.1 in argon. This observed trend in the influence of the background gas appears similar to Allen's findings.

Table 1 *Measured accommodation coefficient for nano-alumina particles with helium, nitrogen, and argon at 300K and 2 atm [15].*

Environment	$\boldsymbol{\alpha}$	Range	$\boldsymbol{\alpha/d_p(nm^{-1})}$
Helium	0.03	$0.015-0.045$	4.6 (10^{-4})
Argon	0.07	$0.035-0.10$	1.0 (10^{-3})
Nitrogen	0.15	$0.12-0.25$	2.2 (10^{-3})

From a molecular dynamics perspective, the accommodation coefficient is primarily influenced by the weight ratio between gas and particles and the gas/surface interaction potential [22]. According to this, the accommodation coefficient in helium is expected to be smaller than that in argon or nitrogen, and this expectation aligns well with Allen's results. Allen, in the previous research [23], experimentally demonstrated that the observed peak temperature significantly exceeds the ambient temperature. This result implies that, instead of the common assumption of an energy accommodation coefficient of unity, the value proposed by Altman, around 0.005, is the only plausible option.

Altman demonstrated that in the simplified lattice model, the accommodation coefficient decreased as the surrounding gas temperature increased until reaching the

minimum value of α_{min}. Afterwards, a further increase in gas temperature led to a slight rise in the accommodation coefficient from α_{min}, reaching an asymptotic value of α_{∞}. This accommodation coefficient value remains relatively constant until the particle reaches its melting point. Altman anticipated a decrease in the accommodation coefficient with increasing ambient temperature, while Goodman, Wachman, and Sipkens argued that the accommodation coefficient is relatively insensitive to particle and ambient temperature [24], [25]. Considering both hypotheses, Allen suggested that if there is a limit at high temperatures, an increase in ambient temperature would either decrease the accommodation coefficient or have little impact. Therefore, Allen claimed that the observed accommodation coefficients are likely close to upper limits for particle temperatures greater than 2300 K.

Since then, there has been very limited experimental exploration regarding the accommodation coefficient of metal and metal oxide nanoparticles. Vander Wal conducted initial tests, demonstrating the sensitivity of the LII method to particle concentration and size across various metal nanoparticles, including tungsten, iron, molybdenum, and titanium [26]. Subsequent researchers have utilized LII to gauge the accommodation coefficient, size distribution, and concentration of specific metal systems. Kock and Eremin conducted two-color TiRe-LII measurements on iron nanoparticles in different gaseous environments [21], [27]. Eremin's findings indicated accommodation coefficients of 0.01, 0.2, and 0.1 for the Fe/He, Fe/CO, and Fe/Ar systems, respectively, significantly lower than those observed for carbon systems (0.44-0.51). Kock reported an accommodation coefficient of 0.13 for both the Fe/Ar and Fe/N2 systems. Murakami et al.

used LII to size molybdenum nanoparticles [28]. Sipkens et al. experimentally investigated the accommodation coefficient of airborne silicon nanoparticles and simulated heat transfer using molecular dynamics [29]. Daun et al. employed molecular dynamics simulations to determine the accommodation coefficient for silicon, molybdenum, and nickel, extending measurements to temperatures beyond the experimental range, a topic to be explored further in this work [30], [28], [29].

The relationship between the accommodation coefficient and temperature has received very little experimental attention. Michelsen [31] attempted to establish a temperature dependence for the accommodation coefficient based on molecular beam data from Hager, Walther, and colleagues [32]–[35], focusing on the interaction of NO with graphite surfaces for application to soot particles. Michelsen observed an exponential decrease in the accommodation coefficient with rising particle temperature [31]. However, the data sets for the NO/graphite system were incomplete, hindering the derivation of an overall accommodation coefficient as a function of gas temperature. Michelsen attempted estimation by linear extrapolating the dataset values, but this method lacked robust evidence beyond the selected dataset [31].

In recent times, high-speed optical imaging techniques have become increasingly advanced for monitoring the spatial and temporal distribution of various atomic and oxide species following the initiation of a laser-induced plasma. These methods have proven effective, particularly for metal-based species forming molecular oxide species in the gas phase, exhibiting easily observable vibrational emission bands. Noteworthy examples include AlO, ZrO/SrO, and UO formation [36] from bulk metal samples, as well as the tracking of other non-oxide molecular species [37]. Investigations have delved into the

impact of laser energy, pulse duration, wavelength, and other modifications of laser conditions on plasma hydrodynamics [38], [39]. Additionally, studies have explored the influence of background gas and pressure, with some focusing on atmospheric laser-induced plasmas [40]–[45]. The effect of particle morphology and size, relevant to energetic materials, has also been examined for materials like concrete [46]. Laser-induced breakdown spectroscopy (LIBS) has found successful applications in characterizing materials relevant to defense communities, including high explosives (HE) and other hazardous materials [47]. Such applications often involve metal and metalloid powders with non-uniform particle size distributions, exhibiting diverse performance behavior based on size [8]. The various sizes of commercially available Al powders were analyzed, revealing earlier and stronger AlO formation from nm-sized Al compared to μm-sized Al, emitting in different locations within the plasma [48]. This study highlighted the interconnected role of plasma hydrodynamics and temperature in the formation of gas phase species and the subsequent energy release by the powders and their products on a microsecond scale. Similarly, the plasma chemistry and reaction dynamics of novel Al/Zr composite powders synthesized via ball milling have been examined in relation to material chemistry for particles of comparable sizes [49]. These findings demonstrated variations in electron density and plasma temperatures correlating with other energetic measurements of the sample [50]. The impact of particle size on plasma plume hydrodynamics using inert Al_2O_3 powders has also been recently explored [51].

Gottfried et al. established a strong correlation between LASEM shock speeds and the energetic properties of explosives, as depicted in **Figure 4**. This involved using a 1064 nm 6 ns pulsed laser, generating a peak power density of $3 \times 10^{10} \mathrm{W/cm^2}$ [20]. The

induced shock position was recorded through Schlieren imaging at a high frame rate of 84,000 fps. Similarly, a robust correlation was observed between LASEM shock speeds and the detonation velocities of explosives. Beyond explosives, researchers have extensively employed LASEM to characterize energetic materials such as aluminum, boron, termites, and other innovative core-shell energetic particles [20], [50], [52]–[56]. Gottfried delved into an examination of the distinctions in excitation between non-energetic and energetic residues utilizing a laser pulse of 900 mJ and 6 ns duration at 1064 nm [54]. Notably, the energy output of the laser pulse in this particular experiment far exceeded the customary pulse energies commonly employed in laser-induced shock experiments, which typically hover around 200 mJ. The outcomes unveiled conspicuous dissimilarities in visible emission, shock structure, and heat-affected zones between inert and energetic materials. The experimental findings showed that for non-metal samples undergoing exothermic reactions upon decomposition, chemical reactions occurring in the vapor plume behind the shock front exerted a discernible influence on the velocity of the shock front. According to these findings, laser-induced plasma emission from energetic materials significantly increased compared to non-energetic materials. Moreover, the laser heating of energetic materials led to larger heat-affected zones in the surrounding atmosphere, promoting the explosive release of particles from the sample surface. This phenomenon led to the formation of supplementary shock fronts and the generation of faster external shock front velocities, measuring 4750 m/s, as opposed to the range of 550–600 m/s observed in non-energetic materials. LASEM experiment demonstrated that the most potent explosive material in Gottfried's study yielded the highest shock velocities. Noteworthy is the extended duration of shock wave position measurement, reaching up to

200 ms, which was achieved by capturing more than fifteen frames for each event. In contrast to earlier laser-induced shock studies on non-energetic materials, the thermal energy within the energetic material vapor plume originated from both the energy transferred from the laser and the subsequent exothermic chemical reactions of the ablated species.

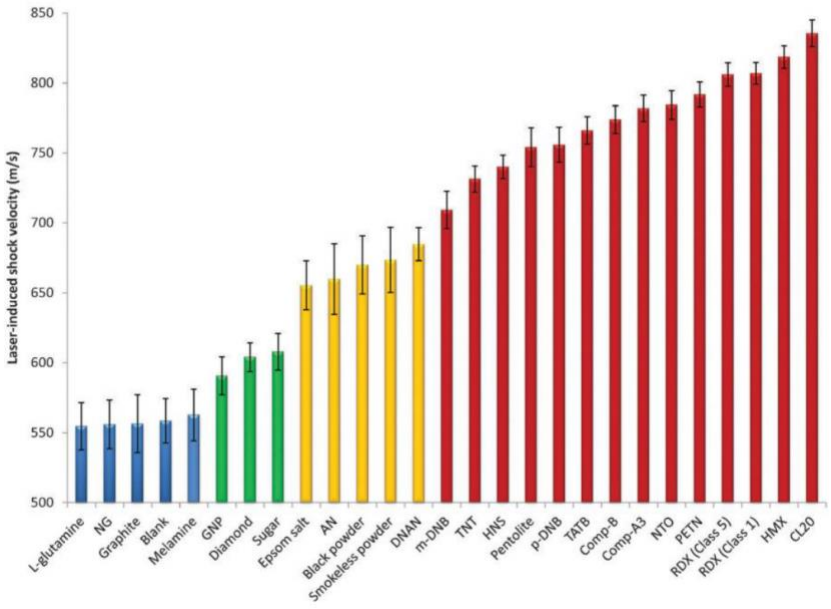

Figure 4 *Characteristic LASEM shock speed of non-energetic and energetic material* [20].

Wainwright et al. [50] utilized LASEM technology to assess the performance of micron-sized 3Al:2Zr, Al:Zr, and Al:3Zr fuel powders, comparing their characteristics to commonly employed Al powder. The ignition of Al/Zr particles via laser-induced plasma was followed by the observation of laser-induced air shock velocities and subsequent shock combustion. Three Al/Zr composite powders (3Al:2Zr, Al:Zr, Al:3Zr), each with mean diameters ranging from 30 to 50 μm, were compared with a 27.3 μm mean diameter Al powder, a frequently used additive in explosive formulations. The laser-induced air shock

velocities for the exclusive fuel composite powders exhibited an approximate 30% increase compared to those of pure Al, suggesting an augmentation in oxidation during the microsecond timescale. Furthermore, these composite powders displayed increased ignition sensitivity and accelerated reaction rates within the 10 to 100 μs timeframe. Unlike aluminum, there was no detectable delay between material combustion immediately post-plasma and the ignition of the deflagration plume. These enhanced reactivity traits indicate the potential applicability of these composites in advanced explosive applications.

1.3 Motivation

As previously mentioned, to model the combustion of aluminum nanoparticles, it is essential to understand the accommodation heat transfer coefficient of alumina. This understanding is crucial for quantifying conduction heat transfer. However, till date, very limited experimental work has been performed to elucidate the accommodation coefficient of aluminum oxide nanoparticle systems. Allen et al. aimed to assess the accommodation heat transfer of aluminum oxide nanoparticles [15]. Nevertheless, Allen's experimental conditions are limited to a small temperature and pressure range, the particle size distribution is overly broad, and the assumptions made during the development of the mathematical framework do not encompass all aspects. Apart from Allen, other existing works suffer from the indirect measurement of particle temperatures. Many of these studies rely on indirect estimation of particle temperature. A direct measurement of the accommodation coefficient is crucial to minimize significant uncertainties [15]. This prompts us to formulate a robust experimental and mathematical methodology for measuring the accommodation heat transfer coefficient of nanoparticles.

While some literature indicates a statistical correlation between LASEM shock speed and detonation velocities of explosives, there is currently no direct evidence confirming the impact of exothermic reactions on shock speed for metal particles. For the exothermic reaction to influence the shock wave, it must occur within the 0-10 μs time scale [57]. This provides an opportunity to measure radicals associated with the exothermic reaction during the early stages, establishing physical evidence for the correlation between LASEM shock speed and detonation velocity. Additionally, it has been suggested that laser power density must exceed $10^{10}\mathrm{W/cm^2}$ to observe any effect on shock speed due to the energetic properties of the target substrate. However, limited evidence exists to support these claims, necessitating further investigation. It is necessary to investigate whether the proposed value of $10^{10}\mathrm{W/cm^2}$ for the laser power density is an appropriate upper limit by conducting LASEM experiments with laser power density lower than the proposed value. Additionally, the precise correlation between exothermic reactions and shockwaves remains unclear. These considerations serve as motivation for the present study.

1.4 Thesis Organization

The current thesis is divided into four chapters, starting with the list of figures and tables, and abbreviations before the main body of the text. The research is centered around two primary themes:

A. measuring the accommodation coefficient of nano alumina particles using laser-induced incandescence (LII)
B. characterizing nano-aluminum (n-Al) particles using laser-induced air shock from energetic material (LASEM) technique.

Chapter 1 provides an overarching overview of both topics, along with a brief introduction to the research themes and a survey of relevant existing research. This chapter also discusses the limitations of existing studies, the motivation behind the research, and outlines the overall thesis organization. It aims to offer a comprehensive understanding of the entire paper, including the rationale for the study and addressing shortcomings identified in previous research.

Chapter 2 delves into the first research theme, providing background knowledge essential for understanding the subject, discussing experimental methods, and presenting conclusions. Moving to Chapter 3, the focus shifts to the second research theme, which similarly includes background knowledge, an explanation of experimental methodologies, discussion of results, and conclusive remarks. Despite their distinct nature, both research themes are interconnected by the overarching goal of particle characterization to comprehend the combustion process mechanism of nano-aluminum.

Finally, Chapter 4 expands on future experiments and outlines ongoing research challenges that require further exploration.

Chapter 2: Measuring the Accommodation Coefficient of Nano Alumina (n-Al_2O_3) Particles using Laser-induced Incandescence (LII) Technique

2.1 Background

To calculate the accommodation coefficient, the particle temperature (T_p) needs to be known. Measuring LII signal and calibration lamp emission at two distinct wavelengths, λ_1 and λ_2, and employing Wien's approximation for blackbody radiation enables the determination of the particle temperature. The subsequent section provides a detailed description of the process for deriving the signal equation for particle temperature. The following outlines a detailed process for deriving a signal equation for the particle temperature and an energy conservation equation. These equations are applicable to experiments measuring the accommodation coefficient of nano-alumina (Al_2O_3) particles. Combining these two equations, the accommodation coefficient can be estimated.

2.1.1 Derivation of The Signal Equation to Measure The Particle Temperature

The spectral emission from a particle is given by

$$E_{p\lambda}(\lambda, T_p) = \tau_p(\lambda) R_{BB}(\lambda, T_p) \varepsilon_p(\lambda, T_p) \tag{2.1}$$

Here, λ is the wavelength and T_p is the temperature of the particle. τ_p is the optical parameter depends on the solid angle and distance from the camera to the event, R_{BB} is the blackbody energy spectral density given by Planck's law, and ε_p is the emissivity of the particles.

Likewise, the spectral emission from the calibration lamp is given by

$$E_{L\lambda}(\lambda, T_L) = \tau_L(\lambda) R_{BB}(\lambda, T_L) \varepsilon_L(\lambda, T_L) \tag{2.2}$$

Here, T_L is the temperature of the calibration lamp, τ_L is the optical parameter of the arrangement used for the lamp, and ε_L is the emissivity of the lamp material.

The blackbody energy spectral density R_{BB} can be derived by Planck's law

$$B_\lambda(\lambda, T) = \frac{2hc^2}{\lambda^5} \frac{1}{e^{\frac{hc}{\lambda K_B T_p}} - 1} \tag{2.3}$$

Planck's law can also be written in terms of the spectral energy density by multiplying B by $\frac{4\pi}{c}$,

$$R_{BB}(\lambda, T_p) = \frac{4\pi}{c} B_\lambda(\lambda, T_p) = \frac{4\pi}{c} \frac{2hc^2}{\lambda^5} \frac{1}{e^{\frac{hc}{\lambda K_B T_p}} - 1} = \frac{4}{c} c_1 \lambda^{-5} \left[exp\left(\frac{c_2}{\lambda T_p}\right) - 1\right]^{-1} \tag{2.4}$$

where $c_1 = 2\pi hc^2$, $c_2 = \frac{hc}{k_B}$, k_B is the Boltzmann constant, c is the speed of light, and h is the Plank's constant.

The spectral distribution of blackbody radiation is described by Plank's law

$$M(\lambda, T) = c_1 \lambda^{-5} \left[exp\left(\frac{c_2}{\lambda T}\right) - 1\right]^{-1} \tag{2.5}$$

The spectral radiance ratio of the blackbody for different wavelengths λ_1 and λ_2 can be written as

$$\frac{M_{\lambda 1,b}}{M_{\lambda 2,b}} = \frac{R_{BB}(\lambda_1, T)}{R_{BB}(\lambda_2, T)} = \frac{c_1 {\lambda_1}^{-5} \left[exp\left(\frac{c_2}{\lambda_1 T}\right) - 1\right]^{-1}}{c_1 {\lambda_2}^{-5} \left[exp\left(\frac{c_2}{\lambda_2 T}\right) - 1\right]^{-1}} = \left(\frac{\lambda_2}{\lambda_1}\right)^5 \frac{\left[exp\left(\frac{c_2}{\lambda_2 T}\right) - 1\right]}{\left[exp\left(\frac{c_2}{\lambda_1 T}\right) - 1\right]} \tag{2.6}$$

At higher frequencies (i.e., lower wavelengths), Plank's law approximately equals the Wien approximation. The following calculation process was carried out to confirm the applicability of the Wien approximation. The calculation utilized the smallest wavelength used in this study, which is 610 nm, and a temperature value of 1500K.

$$\lambda T = \left(610 \times 10^{-9} m\right) \times 1500K = 9.15 \times 10^{-4} m\,K \tag{2.7}$$

$$c_2 \approx 1.4388 \times 10^{-2} m\,K \gg \lambda T \tag{2.8}$$

Therefore, the Wien approximation is applicable as

$$\frac{1}{e^{\frac{c_2}{\lambda T}} - 1} \approx e^{-\frac{c_2}{\lambda T}} \tag{2.9}$$

From **Equation 2.6** and **Equation 2.9**, the spectral radiance ratio of blackbody can be written as

$$\frac{M_{\lambda 1,b}}{M_{\lambda 2,b}} = \frac{R_{BB}(\lambda_1,T)}{R_{BB}(\lambda_2,T)} = \left(\frac{\lambda_2}{\lambda_1}\right)^5 \frac{[exp\left(\frac{c_2}{\lambda_2 T}\right) - 1]}{[exp\left(\frac{c_2}{\lambda_1 T}\right) - 1]} \cong \left(\frac{\lambda_2}{\lambda_1}\right)^5 \frac{[exp\left(\frac{c_2}{\lambda_2 T}\right)]}{[exp\left(\frac{c_2}{\lambda_1 T}\right)]} \tag{2.10}$$

The measurement relies on the hypothesis that the effective radiance for a general body at temperature T can be expressed as the product of blackbody radiance at T times the emissivity. The spectral radiance ratio of general body for T_L and the spectral radiance ratio of general body for T_P can be expressed as

$$\frac{M_{\lambda_1}(T_L)}{M_{\lambda_2}(T_L)} = \frac{\varepsilon_L(\lambda_1,T_L) R_{BB}(\lambda_1,T_L)}{\varepsilon_L(\lambda_2,T_L) R_{BB}(\lambda_2,T_L)} \cong \frac{\varepsilon_L(\lambda_1,T_L)}{\varepsilon_L(\lambda_2,T_L)} \left(\frac{\lambda_2}{\lambda_1}\right)^5 \frac{[exp\left(\frac{c_2}{\lambda_2 T_L}\right)]}{[exp\left(\frac{c_2}{\lambda_1 T_L}\right)]} \tag{2.11}$$

$$\frac{M_{\lambda_1}(T_P)}{M_{\lambda_2}(T_P)} = \frac{\varepsilon_P(\lambda_1,T_P)}{\varepsilon_P(\lambda_2,T_P)} \frac{R_{BB}(\lambda_1,T_p)}{R_{BB}(\lambda_2,T_p)} \cong \frac{\varepsilon_P(\lambda_1,T_P)}{\varepsilon_P(\lambda_2,T_P)} \left(\frac{\lambda_2}{\lambda_1}\right)^5 \frac{[exp\left(\frac{c_2}{\lambda_2 T_p}\right)]}{[exp\left(\frac{c_2}{\lambda_1 T_p}\right)]} \tag{2.12}$$

Divide **Equation 2.11** by **Equation 2.12**

$$\frac{M_{\lambda_1}(T_L)}{M_{\lambda_2}(T_L)} \frac{M_{\lambda_2}(T_P)}{M_{\lambda_1}(T_P)} = \frac{\varepsilon_L(\lambda_1,T_L)}{\varepsilon_L(\lambda_2,T_L)} \frac{\varepsilon_P(\lambda_2,T_P)}{\varepsilon_P(\lambda_1,T_P)} \frac{[exp\left(\frac{c_2}{\lambda_2 T_L}\right)]}{[exp\left(\frac{c_2}{\lambda_1 T_L}\right)]} \frac{[exp\left(\frac{c_2}{\lambda_1 T_p}\right)]}{[exp\left(\frac{c_2}{\lambda_2 T_p}\right)]} \tag{2.13}$$

Taking logarithm for both sides

$$ln\left(\frac{M_{\lambda_1}(T_L)}{M_{\lambda_2}(T_L)} \frac{M_{\lambda_2}(T_P)}{M_{\lambda_1}(T_P)}\right) = ln\left(\frac{\varepsilon_L(\lambda_1,T_L)}{\varepsilon_L(\lambda_2,T_L)} \frac{\varepsilon_P(\lambda_2,T_P)}{\varepsilon_P(\lambda_1,T_P)} \frac{[exp\left(\frac{c_2}{\lambda_2 T_L}\right)]}{[exp\left(\frac{c_2}{\lambda_1 T_L}\right)]} \frac{[exp\left(\frac{c_2}{\lambda_1 T_p}\right)]}{[exp\left(\frac{c_2}{\lambda_2 T_p}\right)]}\right)$$

$$= ln\left(\frac{\varepsilon_L(\lambda_1,T_L)}{\varepsilon_L(\lambda_2,T_L)}\frac{\varepsilon_P(\lambda_2,T_P)}{\varepsilon_P(\lambda_1,T_P)}\right) + c_2\left(\frac{1}{\lambda_2}-\frac{1}{\lambda_1}\right)\frac{1}{T_L} - c_2\left(\frac{1}{\lambda_2}-\frac{1}{\lambda_1}\right)\frac{1}{T_P} \quad (2.14)$$

Rearrange the **Equation 2.14**

$$c_2\left(\frac{1}{\lambda_2}-\frac{1}{\lambda_1}\right)\frac{1}{T_P} = ln\left(\frac{\varepsilon_L(\lambda_1,T_L)}{\varepsilon_L(\lambda_2,T_L)}\frac{\varepsilon_P(\lambda_2,T_P)}{\varepsilon_P(\lambda_1,T_P)}\right) + c_2\left(\frac{1}{\lambda_2}-\frac{1}{\lambda_1}\right)\frac{1}{T_L} - ln\left(\frac{M_{\lambda_1}(T_L)}{M_{\lambda_2}(T_L)}\frac{M_{\lambda_2}(T_P)}{M_{\lambda_1}(T_P)}\right) \quad (2.15)$$

$$T_P = c_2\left(\frac{1}{\lambda_2}-\frac{1}{\lambda_1}\right)\left[ln\left(\frac{\varepsilon_L(\lambda_1,T_L)}{\varepsilon_L(\lambda_2,T_L)}\frac{\varepsilon_P(\lambda_2,T_P)}{\varepsilon_P(\lambda_1,T_P)}\right) + c_2\left(\frac{1}{\lambda_2}-\frac{1}{\lambda_1}\right)\frac{1}{T_L} - ln\left(\frac{M_{\lambda_1}(T_L)}{M_{\lambda_2}(T_L)}\frac{M_{\lambda_2}(T_P)}{M_{\lambda_1}(T_P)}\right)\right]^{-1} \quad (2.16)$$

Using **Equation 2.13** and **Equation 2.16** yields

$$T_P = c_2\left(\frac{1}{\lambda_2}-\frac{1}{\lambda_1}\right)\left[ln\left(\frac{\varepsilon_L(\lambda_1,T_L)}{\varepsilon_L(\lambda_2,T_L)}\frac{\varepsilon_P(\lambda_2,T_P)}{\varepsilon_P(\lambda_1,T_P)}\right) + c_2\left(\frac{1}{\lambda_2}-\frac{1}{\lambda_1}\right)\frac{1}{T_L}\right.$$

$$\left. - ln\left(\frac{\varepsilon_L(\lambda_1,T_L)}{\varepsilon_L(\lambda_2,T_L)}\frac{\varepsilon_P(\lambda_2,T_P)}{\varepsilon_P(\lambda_1,T_P)}\frac{[exp\left(\frac{c_2}{\lambda_2 T_L}\right)]}{[exp\left(\frac{c_2}{\lambda_1 T_L}\right)]}\frac{[exp\left(\frac{c_2}{\lambda_1 T_p}\right)]}{[exp\left(\frac{c_2}{\lambda_2 T_p}\right)]}\right)\right]^{-1}$$

$$= c_2\left(\frac{1}{\lambda_2}-\frac{1}{\lambda_1}\right)\left[c_2\left(\frac{1}{\lambda_2}-\frac{1}{\lambda_1}\right)\frac{1}{T_L} - ln\left(\frac{[exp\left(\frac{c_2}{\lambda_2 T_L}\right)]}{[exp\left(\frac{c_2}{\lambda_1 T_L}\right)]}\frac{[exp\left(\frac{c_2}{\lambda_1 T_p}\right)]}{[exp\left(\frac{c_2}{\lambda_2 T_p}\right)]}\right)\right]^{-1} \quad (2.17)$$

From the **Equation 2.10**,

$$\frac{R_{BB}(\lambda_1,T_L)}{R_{BB}(\lambda_2,T_L)}\frac{R_{BB}(\lambda_2,T_p)}{R_{BB}(\lambda_1,T_p)} = \frac{[exp\left(\frac{c_2}{\lambda_2 T_L}\right)]}{[exp\left(\frac{c_2}{\lambda_1 T_L}\right)]}\frac{[exp\left(\frac{c_2}{\lambda_1 T_P}\right)]}{[exp\left(\frac{c_2}{\lambda_2 T_P}\right)]} \quad (2.18)$$

Using **Equation 2.17** and **Equation 2.18** yields

$$T_P = c_2\left(\frac{1}{\lambda_2}-\frac{1}{\lambda_1}\right)\left[c_2\left(\frac{1}{\lambda_2}-\frac{1}{\lambda_1}\right)\frac{1}{T_L} + ln\left(\frac{R_{BB}(\lambda_1,T_p)}{R_{BB}(\lambda_2,T_p)}\frac{R_{BB}(\lambda_2,T_L)}{R_{BB}(\lambda_1,T_L)}\right)\right]^{-1} \quad (2.19)$$

Since the solid angle and distance from heated alumina particles and calibration lamp are constant,

$$\frac{\tau_p(\lambda_1)}{\tau_p(\lambda_2)} = \frac{\tau_L(\lambda_1)}{\tau_L(\lambda_2)} \quad (2.20)$$

Using **Equation 2.1**, **Equation 2.2** and **Equation 2.20** yields

$$\frac{R_{BB}(\lambda_1,T_p)}{R_{BB}(\lambda_2,T_p)}\frac{R_{BB}(\lambda_2,T_L)}{R_{BB}(\lambda_1,T_L)}=\frac{E_{p\lambda_1}(\lambda_1,T_p)\varepsilon_p(\lambda_2,T_p)}{E_{p\lambda_2}(\lambda_2,T_p)\varepsilon_p(\lambda_1,T_p)}\frac{E_{L\lambda_2}(\lambda_2,T_L)\varepsilon_L(\lambda_1,T_L)}{E_{L\lambda_1}(\lambda_1,T_L)\varepsilon_L(\lambda_2,T_L)} \quad (2.21)$$

Therefore, the **Equation 2.19** can be expressed as

$$T_P=c_2\left(\frac{1}{\lambda_2}-\frac{1}{\lambda_1}\right)\left[c_2\left(\frac{1}{\lambda_2}-\frac{1}{\lambda_1}\right)\frac{1}{T_L}+ln\left(\frac{E_{p\lambda_1}(\lambda_1,T_p)\varepsilon_p(\lambda_2,T_p)}{E_{p\lambda_2}(\lambda_2,T_p)\varepsilon_p(\lambda_1,T_p)}\frac{E_{L\lambda_2}(\lambda_2,T_L)\varepsilon_L(\lambda_1,T_L)}{E_{L\lambda_1}(\lambda_1,T_L)\varepsilon_L(\lambda_2,T_L)}\right)\right]^{-1} \quad (2.22)$$

Since blackbody is used as the lamp for calibration, the $\varepsilon_L(\lambda_1,T_L)$ and $\varepsilon_L(\lambda_2,T_L)$ will be close to unity. Therefore,

$$T_P=c_2\left(\frac{1}{\lambda_2}-\frac{1}{\lambda_1}\right)\left[c_2\left(\frac{1}{\lambda_2}-\frac{1}{\lambda_1}\right)\frac{1}{T_L}+ln\left(\frac{E_{p\lambda_1}(\lambda_1,T_p)\varepsilon_p(\lambda_2,T_p)}{E_{p\lambda_2}(\lambda_2,T_p)\varepsilon_p(\lambda_1,T_p)}\frac{E_{L\lambda_2}(\lambda_2,T_L)}{E_{L\lambda_1}(\lambda_1,T_L)}\right)\right]^{-1} \quad (2.23)$$

or

$$T_P=\frac{hc}{k_B}\left(\frac{1}{\lambda_2}-\frac{1}{\lambda_1}\right)\left[\frac{hc}{k_B}\left(\frac{1}{\lambda_2}-\frac{1}{\lambda_1}\right)\frac{1}{T_L}+ln\left(\frac{E_{p\lambda_1}(\lambda_1,T_p)\varepsilon_p(\lambda_2,T_p)}{E_{p\lambda_2}(\lambda_2,T_p)\varepsilon_p(\lambda_1,T_p)}\frac{E_{L\lambda_2}(\lambda_2,T_L)}{E_{L\lambda_1}(\lambda_1,T_L)}\right)\right]^{-1} \quad (2.24)$$

The two wavelengths are denoted by λ_1 and λ_2, and $E_{p\lambda}(\lambda,T_p)$ refers to detected emission from aluminum oxide particles for each wavelength. $E_{L\lambda}(\lambda,T_L)$ is the recorded intensity of the calibrated lamp emission at the temperature T_L used for calibration and ε_p stands for the emissivity of particles depending on the wavelength and particle temperature [58]. Since the particle temperature is unknown, we have to assume a value and solve it iteratively. Kalman et al. previously showed that a $\lambda^{-1.2}$ approximation (closer to the λ^{-1} predicted by the Rayleigh limit, which is the most common assumption) provides the best fit for Nano-alumina near 2800 and 3100 K [59]. The wrong choice of emissivity assumption can cause an error in temperature greater than 500 K, leading to a dramatic change in the interpreted accommodation coefficient. Therefore, the most significant error source could be the emissivity value of particles.

2.1.2 Heat and Mass Transfer Rates at Nano Scales

At the nanoscale, where particle size is much smaller than the mean free path, the gas cannot be considered a continuous medium. The Knudsen number, Kn, commonly employed to describe such scenario, is defined as the ratio of the mean free path of gas molecules to the particle size

$$Kn = \frac{RT}{\sqrt{2}\pi D_a^2 N_A p D_p} \tag{2.25}$$

where R is the gas constant, T is the temperature, D_a is the diameter of the ambient gas molecule, N_A is the Avogadro's number, p is the pressure, and D_p is the particle diameter. The exchange of heat between the particle and the surrounding gas takes place through conduction and radiation. Employing Fuchs methodology [35], the gas volume is partitioned into two distinct zones: (1) the Knudsen layer, characterized by negligible gas molecule collisions, and (2) the area beyond the Knudsen layer, where molecular collisions play a significant role. Free-molecular effects are confined to the Knudsen layer, while continuum laws govern physicochemical processes outside this layer. Determining the temperatures of model nanoparticles can be achieved by solving the energy conservation equation:

$$mc_p \frac{\partial T}{\partial t} = q_{cond}(t, d_p) + q_{evap}(t, d_p) + q_{rad}(t, d_p) \tag{2.26}$$

$$mc_p \frac{\partial T}{\partial t} = \rho V c_p \frac{\partial T}{\partial t} = \rho \frac{4}{3}\pi \left(\frac{d_p}{2}\right)^3 c_p \frac{dT_p}{dt} = \rho c_p \frac{\pi {d_p}^3}{6} \frac{dT_p}{dt} \tag{2.27}$$

Using **Equation 2.26** and **Equation 2.27**,

$$\rho c_p \frac{\pi {d_p}^3}{6} \frac{dT_p}{dt} = q_{cond}(t, d_p) + q_{evap}(t, d_p) + q_{rad}(t, d_p) \tag{2.28}$$

In **Figure 5**, the particle diameters corresponding to Knudsen numbers of 0.01 and 10 are depicted as a function of gas temperature under three different pressures: 1, 10, and 100 atm. At a pressure of 1 atm and a temperature of 3000 K, the critical particle size, where the continuum approximation becomes invalid, is 70 μm. This size decreases by a factor of 10 when the pressure increases from 1 to 10 atm, and the temperature decreases from 3000 to 300 K. It is evident that continuum models are insufficient for capturing the intricate ignition and combustion features of nano aluminum particles. Hence, assuming a $Kn > 10$ poses no harm and falls within the scope of this research. The rates of conduction heat transfer between the particle and Knudsen layer, q_{cond}, are given by [17],

$$q_{cond} = \alpha\pi d_p^2 \frac{p_a}{8}\sqrt{\frac{8k_B T_a}{\pi m_a}}\left(\frac{\gamma+1}{\gamma-1}\right)\left(1-\frac{T_p}{T_a}\right),\ Kn > 10, \tag{2.29}$$

where α is the accommodation coefficient, d_p is the particle diameter, p_a is the ambient gas pressure, k_B is the Boltzmann constant, m_a is the mass of the ambient gas molecule, γ is the specific heat ratio, T_p is the particle temperature and T_a is the ambient gas temperature.

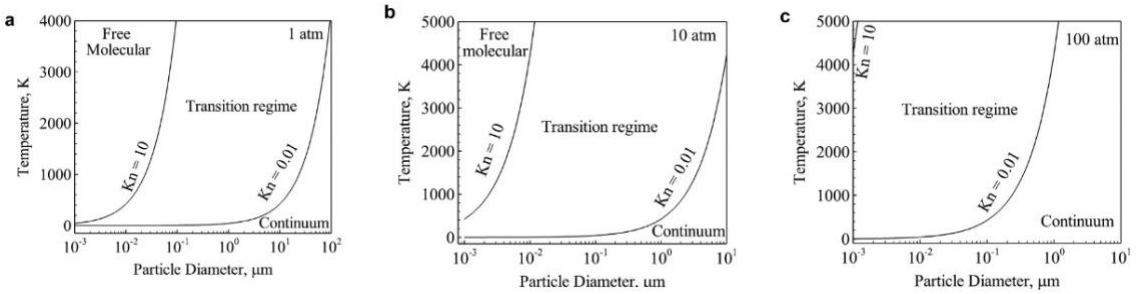

Figure 5 *Particle diameters corresponding to Knudsen numbers of 0.01 and 10 as a function of temperature for three different pressures of 1, 10, and 100 atm* [17].

The Biot number compares the heat transfer resistance within the particle to that at its surface. In **Figure 6**, the impact of particle size on the Biot number of aluminum

particles in air is illustrated for various gas velocities. The temperatures of the particle and gas are 300 K and 1000 K, respectively. Within the relevant particle size range, the calculated Biot numbers are significantly lower than unity, indicating that the resistance to energy diffusion inside the particle is negligible in comparison to the surface heat-transfer resistance. Consequently, temperature gradients inside the particle are minimal, allowing the assumption of internal thermal equilibrium for the particle. This holds true, especially when accounting for free-molecular effects, as the resulting heat transfer coefficient is lower than its continuum counterpart [60]. Additionally, the incorporation of radiation heat transfer does not alter the analysis results. Treating the particle as a lumped system, a single temperature variable proves sufficient for analyzing its ignition and combustion properties.

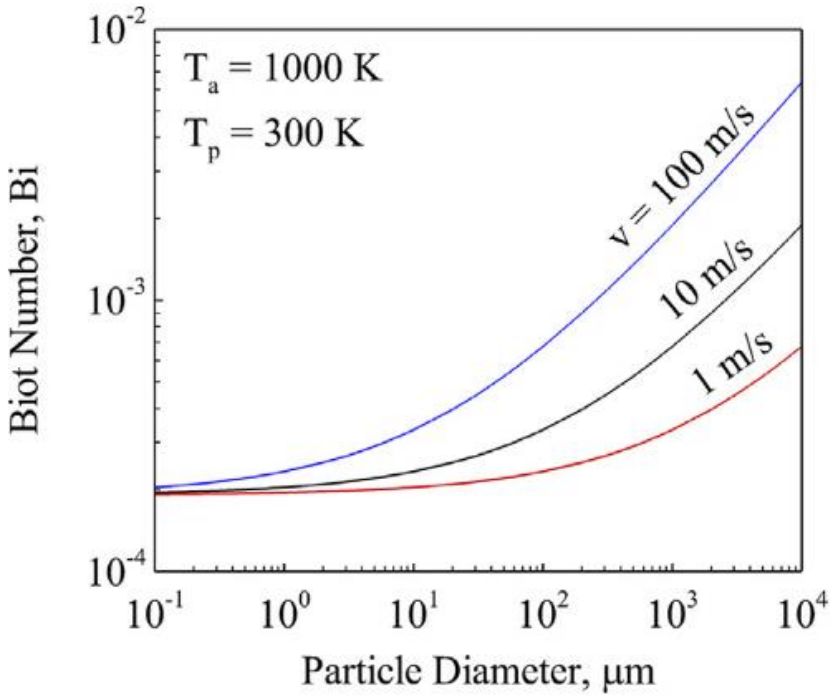

Figure 6 *Biot number of aluminum particles as a function of particle size for different gas velocities* [17].

Figure 7 illustrates the heat transfer rate for each heat transfer mode, assuming a 50 nm alumina particle in 2 atm of N2 at 300 K, reflecting the test conditions in Allen's

work. The analysis assumes an accommodation coefficient of 0.05, subject to reconsideration but conservatively estimated based on previously observed values. The chart clearly indicates that at temperatures below 3000 K, conduction significantly outweighs other heat transfer modes by more than one order of magnitude. Heat loss through evaporation is negligible, constituting less than 1% of the overall heat loss when the particle temperature is below 2500 K. Therefore, monitoring temperature decay below 2500 K, as depicted in **Figure 7**, provides a reliable estimate of the accommodation coefficient in the purely conductive heat loss regime [15].

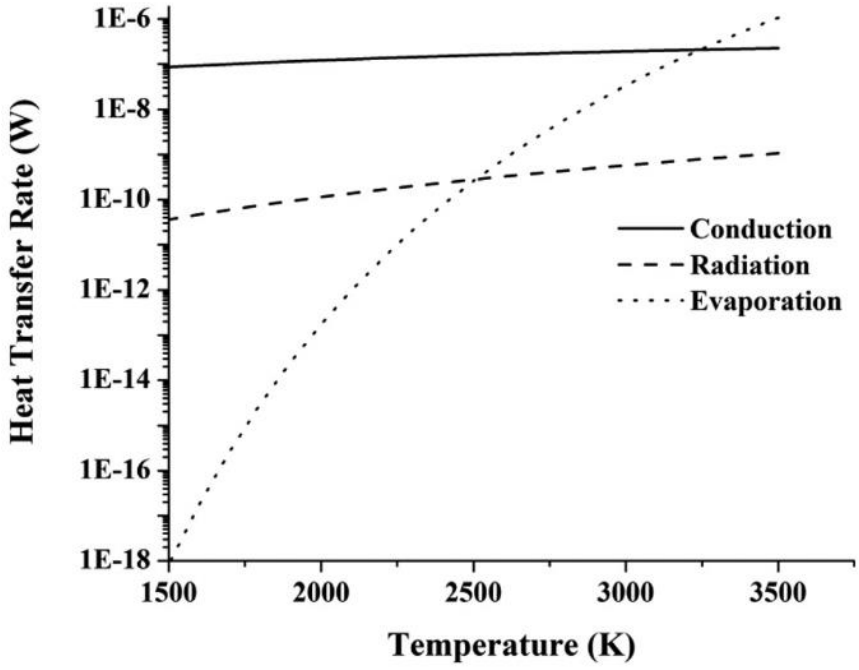

Figure 7 *Heat transfer rates for 50 nm alumina nanoparticles in N2 at 2atm and 300 K assuming α= 0.05* [15].

Disregarding the impact of radiation and evaporation, the energy conservation equation in the Knudsen layer can be revised as follows, considering **Equation 2.28** and **Equation 2.29**.

$$\rho c_p \frac{\pi {d_p}^3}{6} \frac{dT_p}{dt} = \alpha \pi d_p^2 \frac{p_a}{8} \sqrt{\frac{8 k_B T_a}{\pi m_a}} \left(\frac{\gamma+1}{\gamma-1}\right) \left(1 - \frac{T_p}{T_a}\right), \; Kn > 10 \qquad (2.30)$$

When the particle diameter is known, the accommodation coefficient can be calculated by solving both **Equation 2.24** and **Equation 2.30** simultaneously.

2.2 Methodology

2.2.1 Experimental Methods

At large concentrations, nanoparticles frequently exhibit adherence and structure formation, such as agglomeration and coagulation [27]. To disperse nano aluminum oxide powder as individual particles into the gas, a specialized injector was needed. The 4 "x4" x1.8" custom injector housing **(Figure 8)** was designed to withstand high pressure while delivering nano-alumina powder as an evenly and well-dispersed gas/particle mixture to the experiment. The top plate (dark gray) connected the gas tank through an NPT fitting. The nozzle plate (olive green) had 49 tiny holes of 0.04 in diameter. The bottom housing (mustard yellow) had a dome-shaped chamber and an outlet of 0.125 in diameter hole was connected to a tube through an NPT fitting to the main chamber. The three parts were secured together using eight screws, and two O-rings were designed to fit between each part to prevent gas leaks. Two solenoid valves-controlled gas input and output. The bracket was intended to fix the injector to the optical table. The particles were placed in the dome-shaped chamber. High-pressure gas entered into the hemispherical chamber as multiple jet streams through the small holes, allowing the jet gas to disperse the particles and create a uniform gas/particle mixture. Subsequently, the gas/particles were injected into the main pressure vessel. A specially designed 650 cc high-pressure pressure vessel **(Figure 9)** with

high optical accessibility had been utilized. This pressure chamber was equipped with four optical windows (three side windows and one top window).

A planar beam of a pulsed laser with a wavelength of 1064 nm and a duration of 6 ns was directed toward the particles to elevate their temperature. Subsequently, the LII signal was captured using photomultiplier tubes at two distinct wavelengths, as depicted in **Figure 10**. Bandpass filters at 610 nm and 720 nm were chosen based on the quantum efficiency of the PMTs. The recorded LII signal is utilized to track the temperature changes in the nano aluminum oxide particles over a duration of up to 2,500 ns.

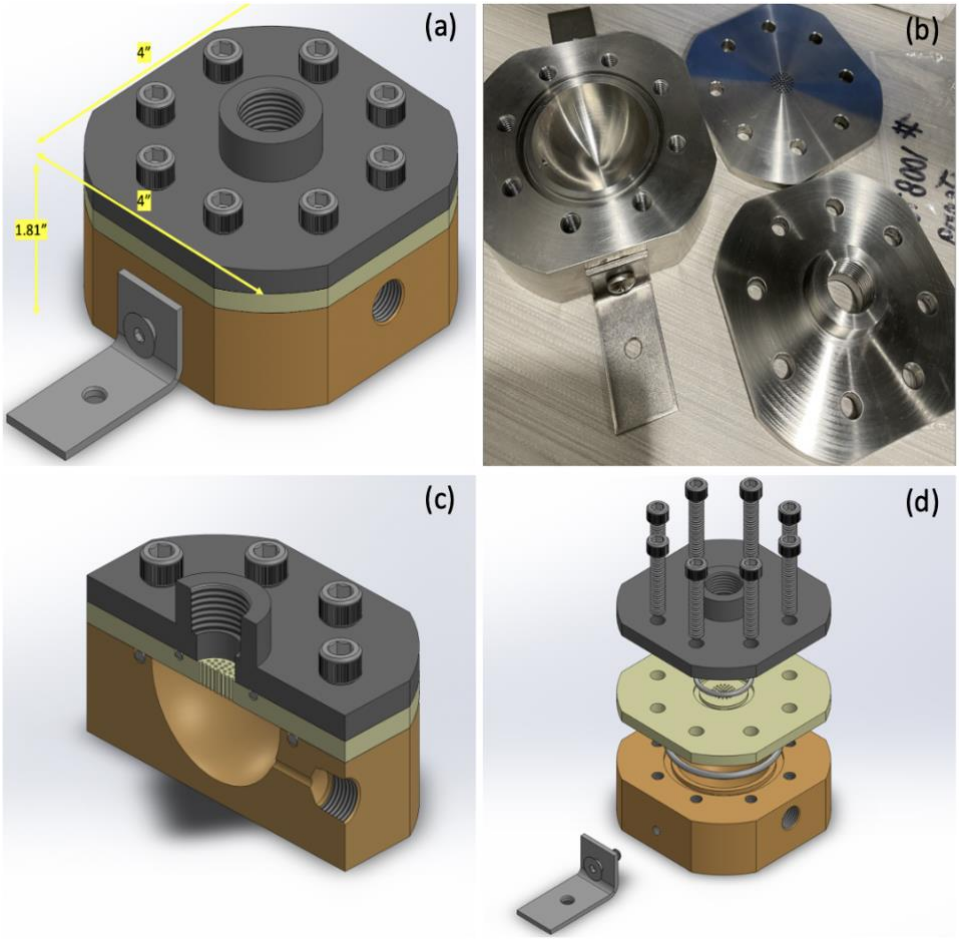

Figure 8 *(a) CAD drawing of the injector, (b) The actual appearance of the injector, (c) Cross-sectional CAD drawing of the injector, (d) Exploded view of the injector.*

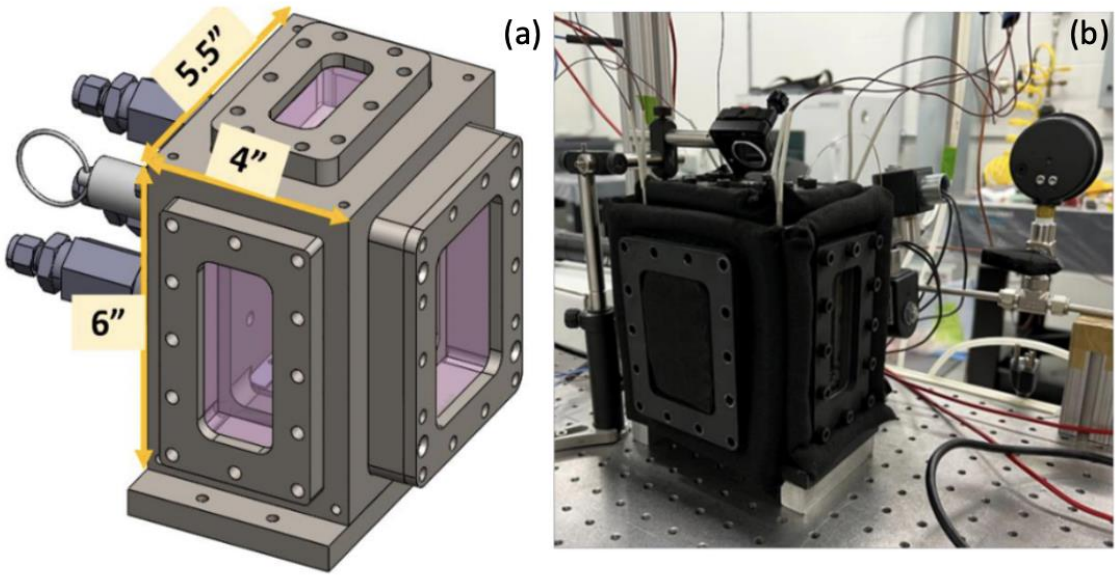

Figure 9 *(a) CAD drawing of the pressure chamber, (b) The actual appeance of the pressure chamber.*

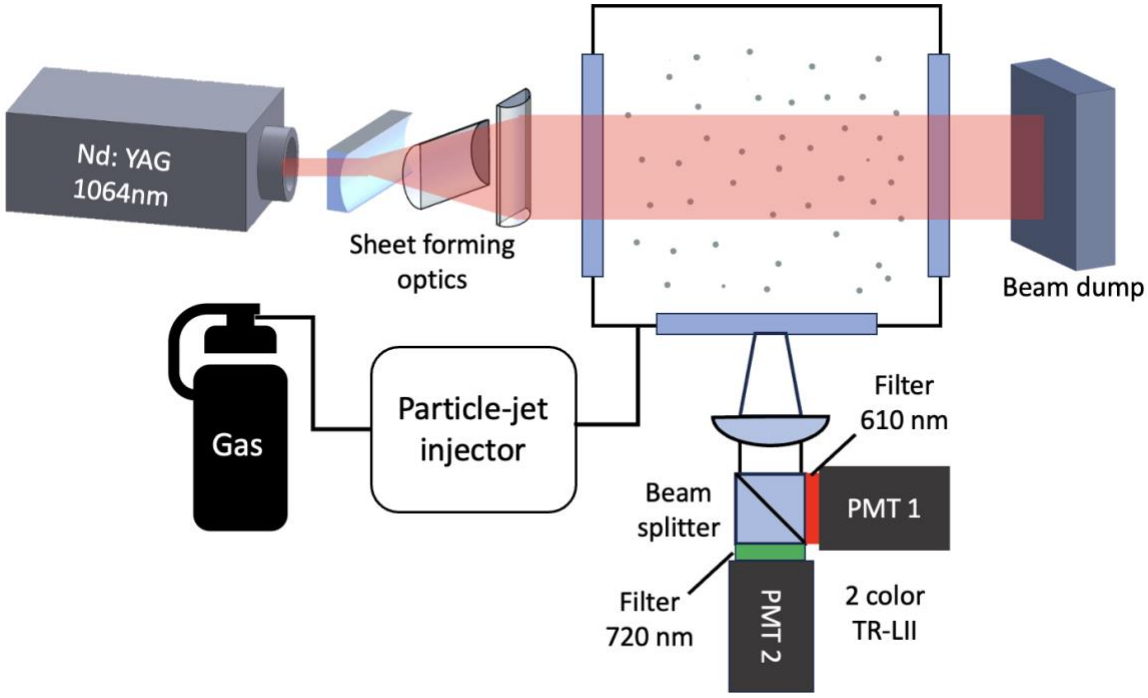

Figure 10 *Schematic of experimental setup.*

2.2.2 Validation of The Derived Signal Equations

To validate the effectiveness of the derived signal equation in this study, the accommodation coefficient was obtained using raw data from the paper by Bejarano et al. [56]. The data from **Figure 11** served as calibration lamp emission values, while the particle's spectral emission values were derived from the signal data at wavelengths of 998 nm and 810 nm in **Figure 12**. Using a in-house MATLAB code, these data values were plugged into **Equation 2.24** to generate a plot depicting particle temperature T_P over time, as depicted in **Figure 13**. The particle temperature plots for each λ^{-1} , $\lambda^{-1.2}$, and $\lambda^{-1.4}$ approximations are illustrated, revealing a temperature difference of approximately ~60-70 K depending on each approximation method. The values from $\lambda^{-1.2}$ approximations, considered the most optimal, as mentioned earlier, were used for subsequent calculations. In **Equation 2.30**, α values of 0.01, 0.02, 0.03, and 0.05 were applied as pre-estimated values, and the calculated particle temperature T_P was substituted to derive the values $\frac{dT_p}{dt}$ for each α value. The initial temperature value and the calculated $\frac{dT_p}{dt}$ were used as slopes to draw fitting plots for each α value, as demonstrated in **Figure 14**. The bold black line represents the experimental T_P graph obtained using the $\lambda^{-1.2}$ approximation. It was observed that the fitting lines $\alpha = 0.02$ the most closely resembled the experimentally obtained T_P plot.

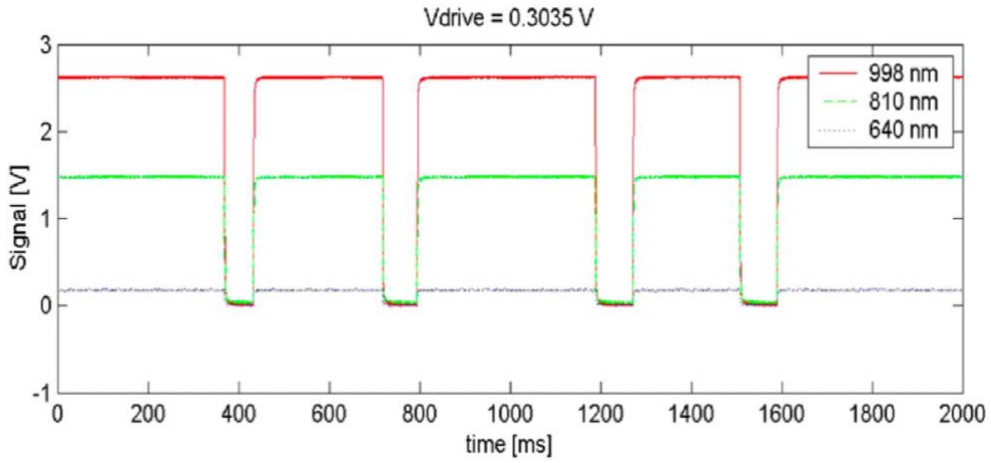

Figure 11 *Typical NIST lamp calibration signals as recorded by the three-color pyrometer (in ascending order 640, 810, and 998 nm) at a corresponding true lamp filament temperature of 2392K* [61].

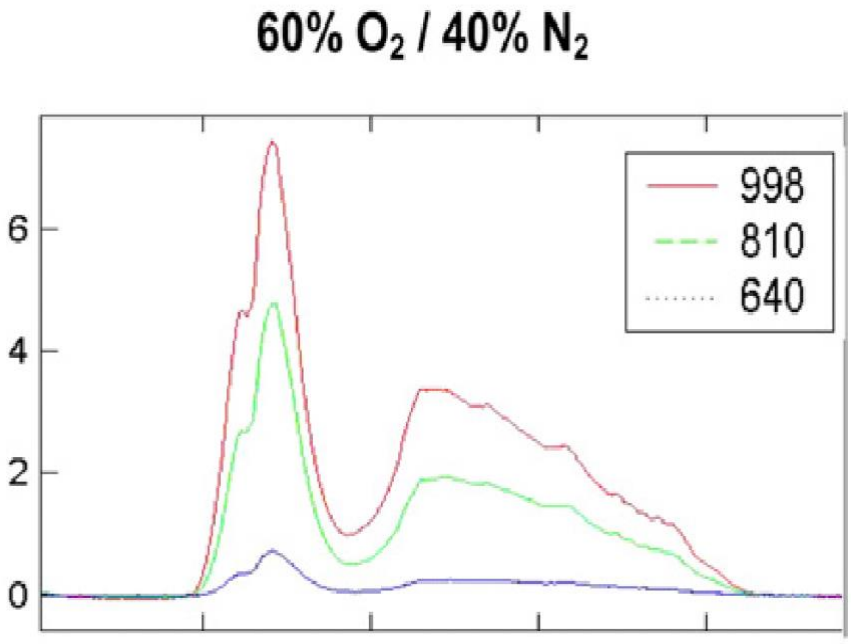

Figure 12 *Pyrometric signals of single bituminous coal particles, 45–53μm, burning in 60% O2–40% N2, at a wall temperature of 1400 K* [61].

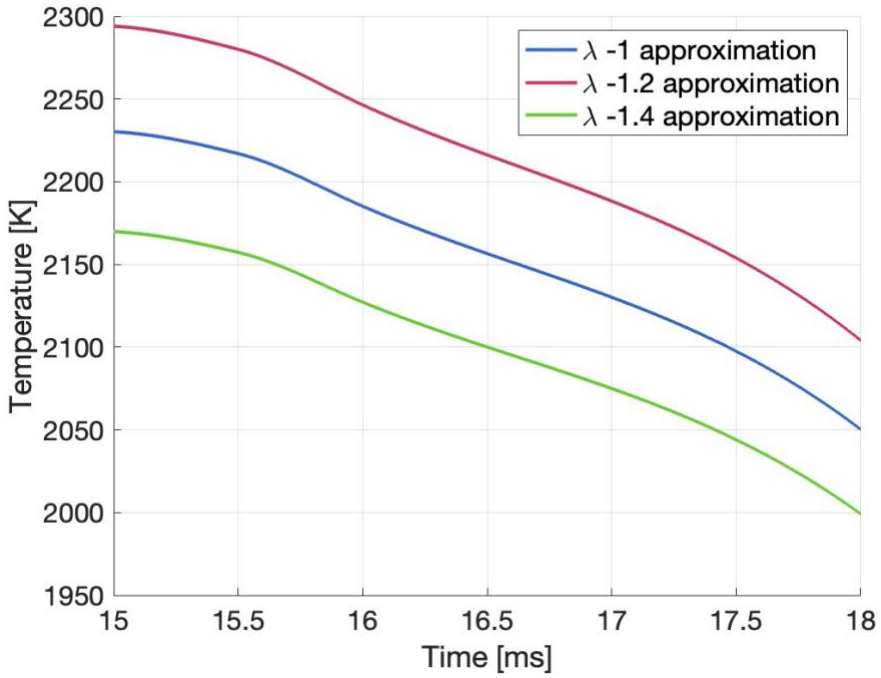

Figure 13 *Plots of particle temperature(Tλ998/λ810) calculated through signal equation, each corresponding to λ^(-1) , λ^(-1.2), and λ^(-1.4) approximation. The calculation used raw data from Bejarano's paper* [61].

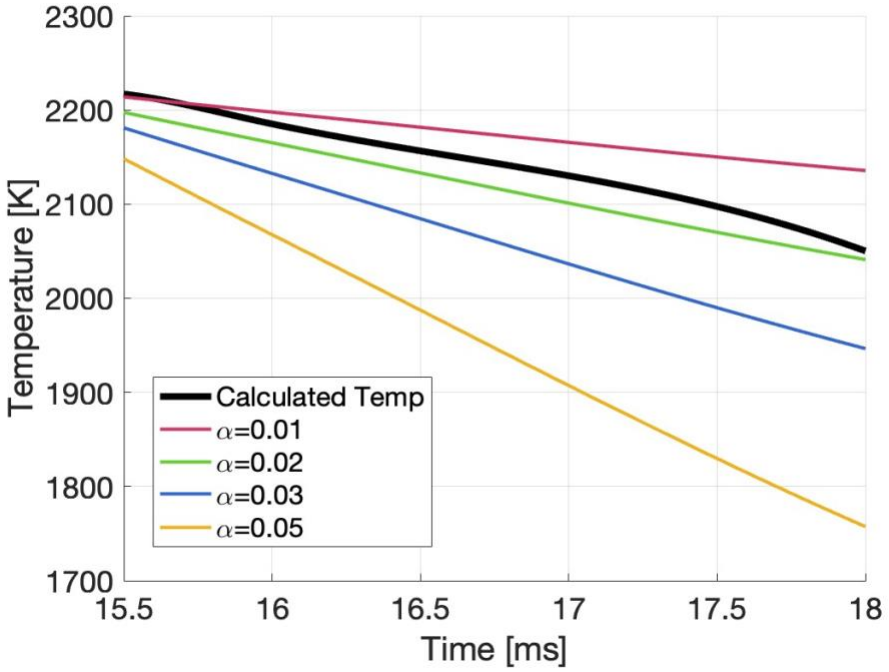

Figure 14 *Calculated Accommodation Coefficient. The Calculated temperature datas (black line) are from Bejarano's paper* [61].

The ideal accommodation coefficient value of 0.02 in the results corresponds reasonably well with the accommodation coefficient values obtained from previous studies on nano particles. It is crucial to highlight that the data used for validating the developed modeling framework pertains to the combustion process of a single coal particle. In the case of nano-alumina, the impact of radiation and evaporation, as mentioned earlier, will be minimal. However, during the combustion process of single coal particles, there is no conclusive evidence to disregard the influence of these two processes. Nevertheless, all presented calculation methods and the devised MATLAB code will be valuably utilized once accommodation coefficient experiments for nano-aluminum particles are conducted in the future.

2.2.3 Results of Calibration Lamp Emissions

An experiment measuring Calibration lamp emission using a candle has been conducted. The utilized filters were set at 750 nm and 830 nm, and the intensity of images captured with a high-speed camera (ix-727) was processed using MATLAB. The corresponding outcomes are illustrated in **Table 2** and **Figure 15**.

Table 2 *Calibration lamp emission for the candlelight and the lamp temperature of the candlelight.*

Lamp Temperature	Average Intensity for $\mathbf{750nm}$	Average Intensity for $\mathbf{830nm}$
1000K	56461	3225

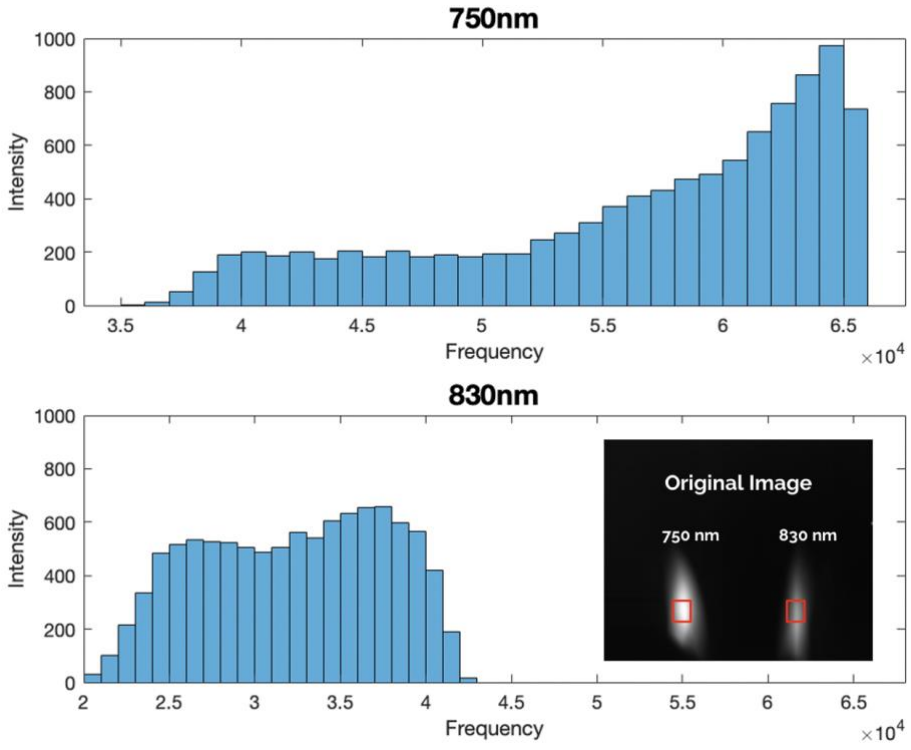

Figure 15 *Histogram of the calibration candlelight emission.*

2.3 Conclusions

A detailed mathematical framework, including the signal equation and assumptions, has been developed and validated, allowing the determination of the accommodation coefficient of nano-sized metal oxide particles using the two-colored LII technique. The model performs extremely well in predicting the accommodation coefficient reported in the literature. A novel experimental setup for measuring the nano-alumina accommodation coefficient has been developed, including the design of a creatively engineered high-pressure injector stream to address the agglomeration issue of nano-alumina particles and to evenly disperse them within the pressure chamber. Although the experiment is currently on hold due to the availability of photomultiplier tubes, it is anticipated that all the suggested frameworks and MATLAB codes will serve as valuable guidance for future

experiments. Detailed descriptions of future work related to this study will be discussed in Chapter 4.

Chapter 3: Characterizing Nano-Aluminum (n-Al) Particles using Laser-induced Air Shock from Energetic Material (LASEM) Technique

3.1 Background

Figure 16 illustrates the sequence of events following the impact of a tightly focused pulsed laser on an energetic material. Initially, the ablated material rapidly undergoes ionization and vaporization, giving rise to the formation of a laser-induced plasma. Subsequently, a shockwave is generated due to the disparity in pressure and temperature compared to the surrounding air. Once the laser pulse is gone (after 6 ns), the plasma begins to cool, but the ongoing exothermic reaction locally sustains elevated temperatures, thereby further augmenting the shock speed. In the millisecond time scale, particles expelled from the target traverse the heated air produced by the plasma and enter the second phase of exothermic reactions.

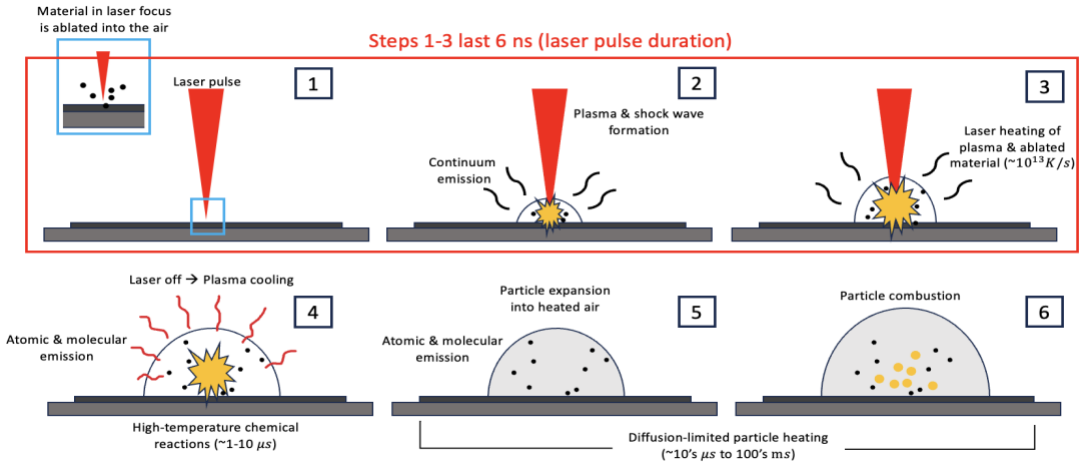

Figure 16 *Sequence of the event following the pulsed laser excitation target substrate deposited with energetic material* [57].

While the primary goal of LASEM is to analyze the relative energetic behavior of materials based on induced air shock speed, it is essential to recognize the significant impact that laser-induced plasma, coupled with exothermic reactions, has on influencing the shock speed. Consequently, it becomes crucial to evaluate the distinct contributions of exothermic reactions to the shock speed.

During the initial interaction between the laser and solid material, processes such as target heating, melting, and vaporization take place. As the pulsed laser removes material, pressure builds up due to the increase in the volume of the ablated particles during their transition from a condensed state to a vapor state. When the laser pulse energies are sufficiently high, phase explosion occurs, causing explosive boiling of the target material beneath the surface layer [20]. This results in mass removal through the ejection of large particles from the sample surface, a process that can continue for hundreds of milliseconds.

The generation of a laser-induced plasma initiates with the absorption of laser energy through inverse bremsstrahlung processes, where photons are absorbed by free electrons, leading to a rapid temperature rise. The hot vapor layer above the sample surface becomes fully ionized at a pressure significantly higher than the ambient pressure. In a region above the sample surface known as the Knudsen layer, atoms, molecules, and ions undergo collisions. Typical plasma temperatures reach tens of thousands of Kelvin, especially for energetic samples, surpassing those of non-energetic materials substantially [62]. Near-infrared laser wavelengths, such as 1064 nm, are particularly effective at heating the plasma compared to visible and ultraviolet wavelengths.

After the laser heating concludes, the plasma undergoes rapid cooling in the first 100 ns. Subsequently, plasma cooling slows down as energy is regained through

recombination and combustion reactions. Thermal energy from the material in the plasma transforms into kinetic energy, resulting in high expansion velocities. The expansion of the high-pressure vapor serves as a piston driving into the surrounding atmosphere, compressing the ambient gas at its front into a thin shell. In the case of laser ablation, the force of this piston depends on the volume of gas produced, which is connected to both the ablated mass and the temperature reached in the plasma plume. Energy is transferred to the surrounding air through a combination of thermal conduction, radiative transfer, and heating by the resulting shock wave. The propagation of the shock wave is determined by the amount of energy released into the plasma state and can be described by the Sedov–Taylor theory [63].

3.2 Methodology

3.2.1 Experimental Methods

A custom-built 650 cc pressure vessel with excellent optical accessibility has been utilized. This pressure chamber is equipped with four optical windows: the upper window directs the laser onto the substrate, the two lateral windows are utilized for schlieren imaging, and the front window enables direct imaging.

LASEM experiments were meticulously conducted, employing nanoparticles of 100 nm Al. A precise loading of 5 mg of Al particles onto a glass slide initiated ignition through a 350 mJ, 6 ns, 1064 nm laser pulse. The laser, focused with precision using a 125 mm focal length planoconvex lens, achieved a power deposition of $1.5 \times 10^9 \mathrm{W/cm^2}$. The Schlieren imaging technique was employed to visualize the laser-induced shock wave. A 1000-watt Xenon arc lamp was utilized as the illumination source, and the light was

focused onto the parabolic mirror using an aspheric condenser lens. Alterations in the air's refractive index, induced by the formation of laser-induced plasma, caused the light rays to bend. Subsequently, when the light was focused beyond another parabolic mirror, a knife edge positioned at the focal spot could selectively block about half of the light rays. As a result, the Schlieren images corresponded to the first spatial derivative of the index of refraction. To capture the variations in the refractive index of air in the test region, a high-speed camera (ix-727) recorded light and dark striations in the images. The imaging of shock waves utilized the following camera settings: 1,000,000 frames per second (fps), 280 ns of shutter time, and a 320 x 20 pixels image size. Additionally, a strategically positioned 102B18 Piezoelectric pressure transducer by PCB captured the relative speed of the shock wave. **Figure 17** presents a simplified schematic of the experimental setup.

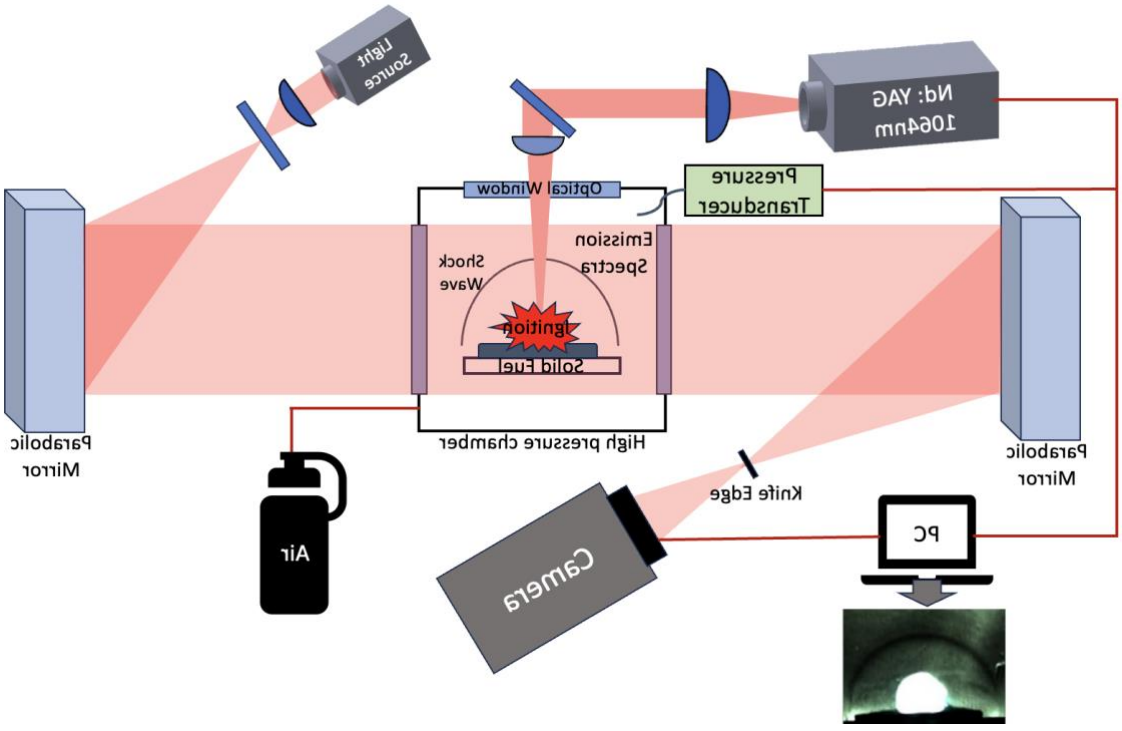

Figure 17 *High-speed Schlieren imaging for measuring time-resolved shock wave position.*

Table 3 *Nd:YAG laser parameters.*

Laser parameter	**Value**
Pulse wavelength λ	1064 nm
Pulse duration t_p	6 ns
Maximum pulse energy E_P	350 mJ
Spot area A	$38.9 \times 10^{-3} \mathrm{cm}^2$
Fluence ε	$9\ \mathrm{J/cm}^2$
Peak power density (irradiance) I	$1.5 \times 10^9 \mathrm{W/cm}^2$

3.3 Results and Discussions

The laser's precise focus on the target anticipated a two-stage combustion process [26]. The first stage, expected within the early 0-10 μs timeframe, results primarily from the vaporization of the target material. Subsequently, the second stage, anticipated in the later millisecond timescale, is triggered by the ignition of ejected material from the target. While this initial investigation did observe direct evidence of second-stage combustion, there remains insufficient proof to definitively conclude that the first-stage combustion occurs within the 0-10 μs timeframe. **Figure 18** displays representative shock images captured using high-speed Schlieren and direct imaging. For the early timeframe of 0-10 μs, the illuminance is primarily dominated by plasma, posing a challenge in drawing definitive conclusions regarding the presence of exothermic reactions during this phase.

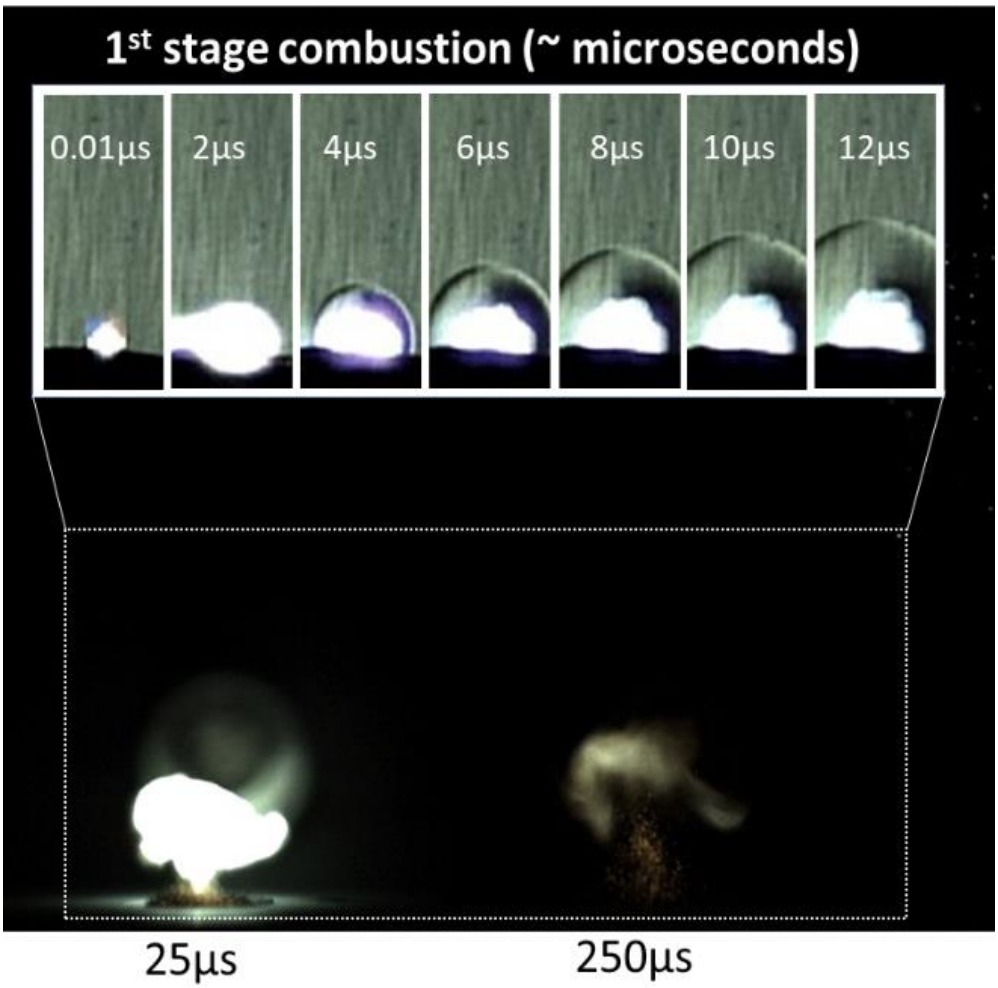

Figure 18 *High-speed schlieren and direct imaging of 100 nm aluminum particles ignited using 6 ns 1064 nm laser pulse.*

In order to furnish supplementary evidence supporting the occurrence of exothermic reactions in the early timeframe, an examination of the shock wave speed was carried out for both aluminum and alumina. When laser-induced heating occurs in target particles, resulting shock waves progress in the direction of the laser source. Upon reaching the pressure transducer situated above the heating location, a signal is generated. **Figure 19 (a)** illustrates the time taken for shock waves produced by pulse lasers under identical experimental conditions to reach the pressure transducer and the corresponding signal magnitudes. In the case of aluminum, the shock waves reach the pressure transducer

approximately 2 µs earlier than those generated from alumina. Additionally, the signal magnitude in aluminum surpasses that in alumina, indicating that the shock waves from aluminum exhibit both greater speed and strength compared to those from alumina.

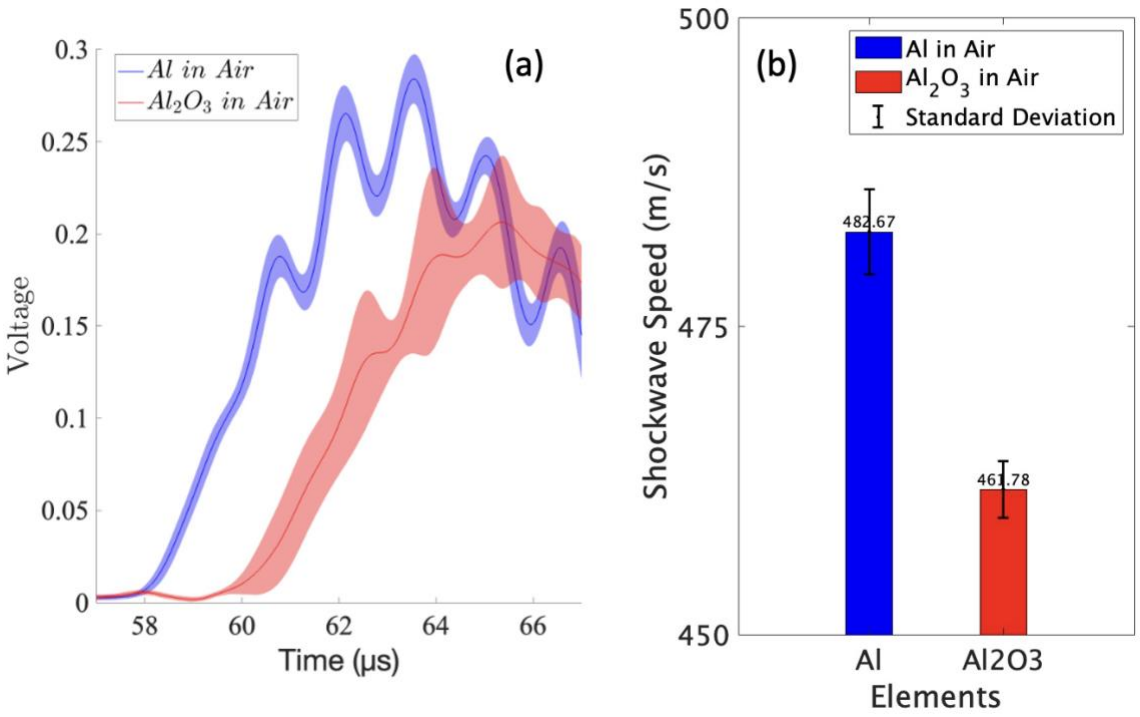

Figure 19 *(a) Time taken by shock wave to reach the pressure transducer. (b) Represents shock speed derived from high-speed Schlieren imaging.*

In **Figure 19 (b)**, the shock wave velocity derived from Schlieren imaging is depicted. The calculation of shock speed involved determining the slope of the linear fit in the position versus time plot, extracted by marking shock fronts on the images. Consistent with the findings from the pressure transducer data, it is observed that the shock wave velocity in aluminum is roughly 20 m/s faster than that in alumina. The observed higher shock wave velocity in aluminum is due to the fact that, unlike the non-energetic substance alumina, the energetic material aluminum undergoes exothermic reactions. This suggests that shock waves are more intense and rapidly generated due to the exothermic reaction in

aluminum. Hence, we can infer that exothermic reactions play a role in the formation of shock waves.

To provide a more comprehensive analysis of the occurrence of exothermic reactions in the initial stages of combustion, an additional experiment was conducted, which is bandpass intensified imaging of Al, AlO and O (**Figure 20**). When a high-power laser is shot, it causes rapid evaporation of the target material, resulting in a signal from aluminum and some ionized gas. This leads to the observation of atomic peaks of oxygen, with the Al-O reacting to form aluminum monoxide (AlO) in the early stages. AlO serves as a signature of an exothermic reaction on Al.

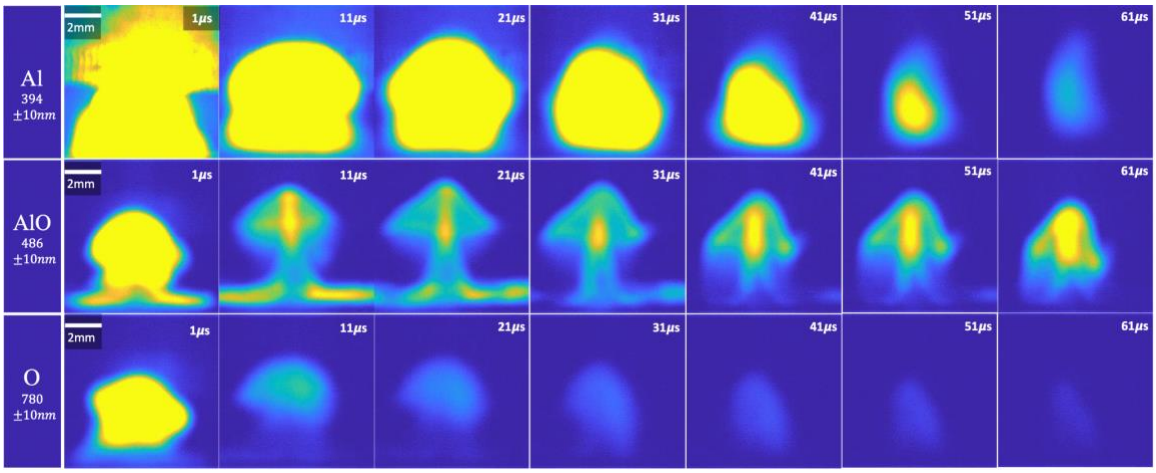

Figure 20 *Imaging of spatiotemporal evolution of Al,AlO,and O. Shutter speed: 200,000 fps, Size: 236 x 234 pixels, Shutter time: 289 ns.*

The laser generates plasma with a high number density of electrons. These electrons collide with aluminum and atomic oxygens, causing these atoms to enter higher electronic excitation states. To obtain individual signals for Al, AlO, and O, three specific wavelength filters were utilized. According to the NIST database, Al, AlO, and O exhibit their most prominent signals at wavelengths of 394 nm, 486 nm, and 780 nm, respectively. Examining the images observed through the AlO filter, it is evident that the signal is vital in the initial

stages (1-11 μs) and gradually diminishes over time. This implies the occurrence of an exothermic reaction in the early stages. We posit that the enhanced shock wave results from the heat released during this exothermic reaction in the early timing scale.

3.4 Conclusions

LASEM experiments were performed on nano-aluminum and nano-alumina particles using air as the background gas. Shockwave velocity information was derived using two approaches: a) detecting shockwave signals through pressure transducers and b) visualizing shockwaves using Schlieren imaging technique. Both sets of results consistently indicated that the shockwave velocity of aluminum surpassed the shockwave velocity of alumina. To probe the presence of exothermic reactions within the early time stage (1-11 μs), laser-induced signals from Al, AlO, and O emissions subsequent to laser irradiation of aluminum particles were measured. The outcomes demonstrated a robust AlO signal during the initial 1-11 ns, gradually diminishing. This serves as compelling evidence for the occurrence of an exothermic reaction in the early temporal stages. Consequently, the hypothesis asserting that the shockwave velocity of aluminum particles is impacted by exothermic reactions has been further affirmed.

Chapter 4: Future Work

4.1 Detailed Study of Accommodation Coefficient Measurements of Various Nanoparticles using LII

Allen et al. used the particle size distribution obtained from Transmission Electron Microscopy (TEM) to determine the accommodation heat coefficient of aluminum oxide particles [10]. However, when aluminum oxide particles are dispersed in air, they tend to form agglomerates and behave as single particle when heated by a laser. As a result, TEM may not accurately represent the particle size present in the aerosol. To address this issue, our goal is to measure particle size in the aerosol using a Differential and Scanning Mobility Particle Sizer (SMPS), as depicted in **Figure 21**. A small flow sample can be extracted from the pressure vessel containing the aluminum oxide aerosol particles and introduced into the SMPS system to assess the particle size distribution before each experiment.

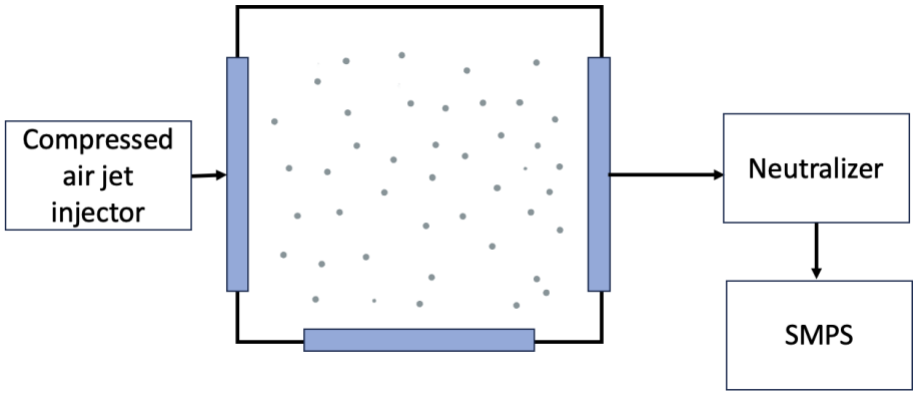

Figure 21 *Schematic of scanning mobility particle sizer system.*

The LII signal will be captured using PMTs at two different wavelengths. Subsequently, utilizing the obtained LII signal information, the mathematical framework developed in

Chapter 2 will be utilized to determine the accommodation coefficient of nanoparticles of various materials (e.g., alumina, iron oxide, cobalt oxide, etc.). A comprehensive database containing these accommodation coefficient values will significantly benefit future research.

4.2 Extend the LASEM Technique to Other Energetic Metals

Renewed interest in metal combustion has arisen primarily due to the current capability to consistently create and analyze metallic nanoparticles. Moreover, the long-term potential of nanotechnology offers the prospect of unparalleled control over the structure of reactive and energetic materials across a broad range of length scales, from nanometers to meters [8]. The favorable characteristics of nano-sized metal powders in combustion systems are often ascribed to their elevated specific surface area, leading to heightened reactivity, and their inherent capacity to store energy on surfaces. The LASEM technique, a relatively recent method for characterizing metal nanoparticles, should be investigated further to examine other energetic metals like boron, magnesium, titanium, molybdenum, etc. Numerous significant metal materials, including titanium and magnesium, exist beyond aluminum. The heat transfer and combustion characterizing of nanoparticles derived from these metals are actively under investigation. We will extend the LASEM experiments to include these nano-metal particles other than aluminum. These investigations are planned for the future.

We also aim to enhance the accuracy of the estimation by improving sensitivity and the quality of imaging. We intend to enhance the quality of shock imaging by employing a 400 W, 10 ns pulsed 640 nm diode laser as the Schlieren light source. Additionally, we

will integrate a magnifying lens on the camera to augment the mm/pixel resolution and eliminate any interference from plasma emissions that might obscure the shock imaging.

Examining the AlO-filtered image in **Figure 20**, we observed a robust signal in the initial 1-11 ns, followed by a gradual decline and a subsequent signal resurgence from 41ns onwards. Additional investigation is necessary to comprehend the underlying factors influencing these outcomes.

References

[1] C. Kong, Q. Yao, D. Yu, and S. Li, “Combustion characteristics of well-dispersed aluminum nanoparticle streams in post flame environment,” *Proc. Combust. Inst.*, vol. 35, no. 2, pp. 2479–2486, 2015, doi: 10.1016/j.proci.2014.06.127.

[2] D. S. Sundaram, V. Yang, and V. E. Zarko, “Combustion of nano aluminum particles (Review),” *Combust. Explos. Shock Waves*, vol. 51, no. 2, pp. 173–196, 2015, doi: 10.1134/S0010508215020045.

[3] A. Ingenito and C. Bruno, “Using aluminum for space propulsion,” *J. Propuls. Power*, vol. 20, no. 6, pp. 1056–1063, 2004, doi: 10.2514/1.5132.

[4] R. G. Sarawadekar and J. P. Agrawal, “Nanomaterials in pyrotechnics,” *Def. Sci. J.*, vol. 58, no. 4, pp. 486–495, 2008, doi: 10.14429/dsj.58.1669.

[5] K. Mahmoodi and B. Alinejad, “Enhancement of hydrogen generation rate in reaction of aluminum with water,” *Int. J. Hydrogen Energy*, vol. 35, no. 11, pp. 5227–5232, 2010, doi: 10.1016/j.ijhydene.2010.03.016.

[6] G. A. Risha, B. J. Evans, E. Boyer, R. B. Wehrman, K. K. Kuo, and N. Engineering, “NANO-SIZED ALUMINUM- AND BORON-BASED SOLID-FUEL CHARACTERIZATION IN A HYBRID ROCKET ENGINE,” *39th AIAA/ASME/SAE/ASEE Jt. Propuls. Conf. Exhib.*, no. July, pp. 1–14, 2003.

[7] Y. Huang, G. A. Risha, V. Yang, and R. A. Yetter, “Effect of particle size on combustion of aluminum particle dust in air,” *Combust. Flame*, vol. 156, no. 1, pp. 5–13, 2009, doi: 10.1016/j.combustflame.2008.07.018.

[8] R. A. Yetter, G. A. Risha, and S. F. Son, “Metal particle combustion and

nanotechnology," *Proc. Combust. Inst.*, vol. 32 II, no. 2, pp. 1819–1838, 2009, doi: 10.1016/j.proci.2008.08.013.

[9] N. Cabrera and N. F. Mott, "Theory of the oxidation of metals," *Reports Prog. Phys.*, vol. 12, no. 1, pp. 163–184, 1949, doi: 10.1088/0034-4885/12/1/308.

[10] K. Lutton and J. R. Scully, "Kinetics of oxide growth of passive films on transition metals," *Encycl. Interfacial Chem. Surf. Sci. Electrochem.*, pp. 284–290, 2018, doi: 10.1016/B978-0-12-409547-2.13576-0.

[11] D. Laboureur, G. Glabeke, and J. B. Gouriet, "Validation of Cabrera-Mott model for low-temperature oxidation of aluminum nanoparticles," *J. Nanoparticle Res.*, vol. 23, no. 3, 2021, doi: 10.1007/s11051-021-05170-z.

[12] K. J. Daun and S. C. Huberman, "Influence of particle curvature on transition regime heat conduction from aerosolized nanoparticles," *Int. J. Heat Mass Transf.*, vol. 55, no. 25–26, pp. 7668–7676, 2012, doi: 10.1016/j.ijheatmasstransfer.2012.07.076.

[13] F. Liu, K. J. Daun, D. R. Snelling, and G. J. Smallwood, "Heat conduction from a spherical nano-particle: Status of modeling heat conduction in laser-induced incandescence," *Appl. Phys. B Lasers Opt.*, vol. 83, no. 3, pp. 355–382, 2006, doi: 10.1007/s00340-006-2194-1.

[14] I. S. Altman, "High-Temperature estimation of energy accommodation coefficient of gas molecules on the surface," *J. Phys. Stud.*, 1999.

[15] D. Allen, H. Krier, and N. Glumac, "Nano-Alumina Accommodation Coefficient Measurement Using Time-Resolved Laser-Induced Incandescence," *J. Heat Transfer*, vol. 138, no. 11, pp. 1–8, 2016, doi: 10.1115/1.4033642.

[16] F. Liu, G. J. Smallwood, and D. R. Snelling, "Effects of primary particle diameter

and aggregate size distribution on the temperature of soot particles heated by pulsed lasers," *J. Quant. Spectrosc. Radiat. Transf.*, vol. 93, no. 1-3 SPEC. ISS., pp. 301–312, 2005, doi: 10.1016/j.jqsrt.2004.08.027.

[17] D. S. Sundaram, P. Puri, and V. Yang, "A general theory of ignition and combustion of nano- and micron-sized aluminum particles," *Combust. Flame*, vol. 169, pp. 94–109, 2016, doi: 10.1016/j.combustflame.2016.04.005.

[18] V. Glasziou, G. Legros, C. Chauveau, S. Courtiaud, and O. France, "Temperature measurement during the combustion of a single aluminium particle," *Proc. 29th ICDERS Conf.*, pp. 1–5, 2023.

[19] Z. Lv, Z. X. Xia, B. Liu, and Y. C. Liu, "Experimental and numerical investigation of a solid-fuel rocket scramjet combustor," *J. Propuls. Power*, vol. 32, no. 2, pp. 273–278, 2016, doi: 10.2514/1.B35838.

[20] J. L. Gottfried, "Influence of exothermic chemical reactions on laser-induced shock waves," *Phys. Chem. Chem. Phys.*, vol. 16, no. 39, pp. 21452–21466, 2014, doi: 10.1039/c4cp02903h.

[21] A. Eremin, E. Gurentsov, and C. Schulz, "Influence of the bath gas on the condensation of supersaturated iron atom vapour at room temperature," *J. Phys. D. Appl. Phys.*, vol. 41, no. 5, 2008, doi: 10.1088/0022-3727/41/5/055203.

[22] K. J. Daun, T. A. Sipkens, J. T. Titantah, and M. Karttunen, "Thermal accommodation coefficients for laser-induced incandescence sizing of metal nanoparticles in monatomic gases," *Appl. Phys. B Lasers Opt.*, vol. 112, no. 3, pp. 409–420, 2013, doi: 10.1007/s00340-013-5508-0.

[23] D. Allen, H. Krier, and N. Glumac, "Heat transfer effects in nano-aluminum

combustion at high temperatures," *Combust. Flame*, vol. 161, no. 1, pp. 295–302, 2014, doi: 10.1016/j.combustflame.2013.07.010.

[24] F. O. Goodman and H. Y. Wachman, "Formula for thermal accommodation coefficients," *J. Chem. Phys.*, vol. 46, no. 6, pp. 2376–2386, 1967, doi: 10.1063/1.1841046.

[25] T. A. Sipkens *et al.*, "In situ nanoparticle size measurements of gas-borne silicon nanoparticles by time-resolved laser-induced incandescence," *Appl. Phys. B Lasers Opt.*, vol. 116, no. 3, pp. 623–636, 2014, doi: 10.1007/s00340-013-5745-2.

[26] R. L. Vander Wal, T. M. Ticich, and J. R. West, "Laser-induced incandescence applied to metal nanostructures," *Appl. Opt.*, vol. 38, no. 27, p. 5867, 1999, doi: 10.1364/ao.38.005867.

[27] B. F. Kock, C. Kayan, J. Knipping, H. R. Orthner, and P. Roth, "Comparison of LII and TEM sizing during synthesis of iron particle chains," *Proc. Combust. Inst.*, vol. 30, no. 1, pp. 1689–1697, 2005, doi: 10.1016/j.proci.2004.07.034.

[28] Y. Murakami, T. Sugatani, and Y. Nosaka, "Laser-induced incandescence study on the metal aerosol particles as the effect of the surrounding gas medium," *J. Phys. Chem. A*, vol. 109, no. 40, pp. 8994–9000, 2005, doi: 10.1021/jp058044n.

[29] T. Sipkens, G. Joshi, K. J. Daun, and Y. Murakami, "Sizing of molybdenum nanoparticles using time-resolved laser-induced incandescence," *J. Heat Transfer*, vol. 135, no. 5, pp. 1–8, 2013, doi: 10.1115/1.4023227.

[30] K. J. Daun, "Thermal accommodation coefficients between polyatomic gas molecules and soot in laser-induced incandescence experiments," *Int. J. Heat Mass Transf.*, vol. 52, no. 21–22, pp. 5081–5089, 2009, doi:

10.1016/j.ijheatmasstransfer.2009.05.006.

[31] H. A. Michelsen, “Derivation of a temperature-dependent accommodation coefficient for use in modeling laser-induced incandescence of soot,” *Appl. Phys. B Lasers Opt.*, vol. 94, no. 1, pp. 103–117, 2009, doi: 10.1007/s00340-008-3278-x.

[32] J. Häger, D. Glatzer, H. Kuze, M. Fink, and H. Walther, “Rotationally excited NO molecules incident on a graphite surface: molecular rotation and translation after scattering,” *Surf. Sci.*, vol. 374, no. 1, pp. 181–190, 1997, doi: https://doi.org/10.1016/S0039-6028(96)01212-5.

[33] J. Hager, Y. R. Shen, and H. Walther, “State-selective velocity and angular distributions of NO molecules scattered from a graphite surface,” *Phys. Rev. A*, vol. 31, no. 3, pp. 1962–1964, Mar. 1985, doi: 10.1103/PhysRevA.31.1962.

[34] H. Kuze, J. Häger, and H. Walther, “Influence of scattering history and out-of-plane scattering on the rotational energy redistribution: No scattered from graphite,” *Chem. Phys. Lett.*, vol. 153, no. 6, pp. 569–573, 1988, doi: https://doi.org/10.1016/0009-2614(88)85262-X.

[35] J. Hager and H. Walther, “Use of Laser Techniques to Study the Dynamics of Molecule-Surface Interaction,” *Annu. Rev. Mater. Sci.*, vol. 19, no. 1, pp. 265–293, 1989, doi: 10.1146/annurev.ms.19.080189.001405.

[36] E. J. Kautz *et al.*, “Optical spectroscopy and modeling of uranium gas-phase oxidation: Progress and perspectives,” *Spectrochim. Acta - Part B At. Spectrosc.*, vol. 185, no. July, p. 106283, 2021, doi: 10.1016/j.sab.2021.106283.

[37] M. Gaft, L. Nagli, N. Eliezer, Y. Groisman, and O. Forni, “Elemental analysis of halogens using molecular emission by laser-induced breakdown spectroscopy in air,”

Spectrochim. Acta - Part B At. Spectrosc., vol. 98, pp. 39–47, 2014, doi: 10.1016/j.sab.2014.05.011.

[38] A. Alberti *et al.*, "Laser-induced non-equilibrium plasma kernel dynamics," *J. Phys. D. Appl. Phys.*, vol. 53, no. 2, 2020, doi: 10.1088/1361-6463/ab492a.

[39] M. Thiyagarajan and K. Williamson, "Experimental investigation of 1064 nm IR laser induced plasmas in gases and in liquids," *2013 Abstr. IEEE Int. Conf. Plasma Sci.*, vol. 10, no. 10, pp. 1–1, 2013, doi: 10.1109/plasma.2013.6634784.

[40] J. F. Y. Gravel and D. Boudreau, "Study by focused shadowgraphy of the effect of laser irradiance on laser-induced plasma formation and ablation rate in various gases," *Spectrochim. Acta - Part B At. Spectrosc.*, vol. 64, no. 1, pp. 56–66, 2009, doi: 10.1016/j.sab.2008.10.037.

[41] J. S. Cowpe, J. S. Astin, R. D. Pilkington, and A. E. Hill, "Temporally resolved laser induced plasma diagnostics of single crystal silicon - Effects of ambient pressure," *Spectrochim. Acta - Part B At. Spectrosc.*, vol. 63, no. 10, pp. 1066–1071, 2008, doi: 10.1016/j.sab.2008.09.007.

[42] L. Peter and R. Noll, "Material ablation and plasma state for single and collinear double pulses interacting with iron samples at ambient gas pressures below 1 bar," *Appl. Phys. B Lasers Opt.*, vol. 86, no. 1, pp. 159–167, 2007, doi: 10.1007/s00340-006-2443-3.

[43] Q. L. Ma *et al.*, "Temporal and spatial dynamics of laser-induced aluminum plasma in argon background at atmospheric pressure: Interplay with the ambient gas," *Spectrochim. Acta - Part B At. Spectrosc.*, vol. 65, no. 11, pp. 896–907, 2010, doi: 10.1016/j.sab.2010.08.005.

[44] X. Bai *et al.*, “Convoluted effect of laser fluence and pulse duration on the property of a nanosecond laser-induced plasma into an argon ambient gas at the atmospheric pressure,” *J. Appl. Phys.*, vol. 113, no. 1, 2013, doi: 10.1063/1.4772787.

[45] T. A. Schmitz, J. Koch, D. Günther, and R. Zenobi, “Characterization of aerosol plumes in nanosecond laser ablation of molecular solids at atmospheric pressure,” *Appl. Phys. B Lasers Opt.*, vol. 100, no. 3, pp. 521–533, 2010, doi: 10.1007/s00340-010-4112-9.

[46] C. Gottlieb *et al.*, “Investigation of grain sizes in cement-based materials and their influence on laser-induced plasmas by shadowgraphy and plasma imaging,” *Spectrochim. Acta - Part B At. Spectrosc.*, vol. 165, no. January, p. 105772, 2020, doi: 10.1016/j.sab.2020.105772.

[47] C. Bohling *et al.*, “All-fiber-coupled laser-induced breakdown spectroscopy sensor for hazardous materials analysis,” *Spectrochim. Acta - Part B At. Spectrosc.*, vol. 62, no. 12, pp. 1519–1527, 2007, doi: 10.1016/j.sab.2007.10.038.

[48] E. R. Wainwright, S. W. Dean, F. C. De Lucia, T. P. Weihs, and J. L. Gottfried, “Effect of sample morphology on the spectral and spatiotemporal characteristics of laser-induced plasmas from aluminum,” *Appl. Phys. A Mater. Sci. Process.*, vol. 126, no. 2, pp. 1–18, 2020, doi: 10.1007/s00339-019-3201-9.

[49] E. R. Wainwright, F. De Lucia, T. P. Weihs, and J. L. Gottfried, “Spatiotemporal and emission characteristics of laser-induced plasmas from aluminum-zirconium composite powders,” *Spectrochim. Acta - Part B At. Spectrosc.*, vol. 183, no. May, p. 106270, 2021, doi: 10.1016/j.sab.2021.106270.

[50] E. R. Wainwright, S. W. Dean, S. Vummidi Lakshman, T. P. Weihs, and J. L.

Gottfried, “Evaluating compositional effects on the laser-induced combustion and shock velocities of Al/Zr-based composite fuels,” *Combust. Flame*, vol. 213, pp. 357–368, 2020, doi: 10.1016/j.combustflame.2019.12.009.

[51] C. J. Miller, E. R. Wainwright, J. L. Gottfried, J. Abraham, L. Wei, and M. L. Pantoya, “The influence of particle size on the fluid dynamics of a laser-induced plasma,” *Phys. Fluids*, vol. 34, no. 5, 2022, doi: 10.1063/5.0087569.

[52] J. L. Gottfried, D. K. Smith, C. C. Wu, and M. L. Pantoya, “Improving the Explosive Performance of Aluminum Nanoparticles with Aluminum Iodate Hexahydrate (AIH),” *Sci. Rep.*, vol. 8, no. 1, pp. 1–12, 2018, doi: 10.1038/s41598-018-26390-9.

[53] J. L. Gottfried, E. R. Wainwright, S. Huang, Y. Jiang, and X. Zheng, “Probing boron thermite energy release at rapid heating rates,” *Combust. Flame*, vol. 231, p. 111491, 2021, doi: 10.1016/j.combustflame.2021.111491.

[54] E. R. Wainwright, C. J. Miller, L. Giri, R. A. Pesce-Rodriguez, C. C. Wu, and J. L. Gottfried, “Influence of silicon particle morphology on laser-induced plasma properties,” *Spectrochim. Acta - Part B At. Spectrosc.*, vol. 199, no. October 2022, p. 106597, 2023, doi: 10.1016/j.sab.2022.106597.

[55] J. L. Gottfried, S. W. Dean, C. C. Wu, and F. C. de Lucia, “Measuring fast and slow energy release from aluminum powders,” *AIP Conf. Proc.*, vol. 2272, 2020, doi: 10.1063/12.0000858.

[56] Y. Jiang *et al.*, “Energetic Performance of Optically Activated Aluminum/Graphene Oxide Composites,” *ACS Nano*, vol. 12, no. 11, pp. 11366–11375, 2018, doi: 10.1021/acsnano.8b06217.

[57] J. L. Gottfried and B. C. Barnes, “Higher Time-Resolution LASEM , Part II :

Influence of Plasma Chemistry on the Laser- Induced Shock Waves of Explosives," 2020.

[58] P. Lynch, H. Krier, and N. Glumac, "Emissivity of aluminum-oxide particle clouds: Application to pyrometry of explosive fireballs," *J. Thermophys. Heat Transf.*, vol. 24, no. 2, pp. 301–308, 2010, doi: 10.2514/1.43853.

[59] J. Kalman, D. Allen, N. Glumac, and H. Krier, "Optical depth effects on aluminum oxide spectral emissivity," *J. Thermophys. Heat Transf.*, vol. 29, no. 1, pp. 74–82, 2015, doi: 10.2514/1.T4260.

[60] A. V. Filippov and D. E. Rosner, "Energy transfer between an aerosol particle and gas at high temperature ratios in the Knudsen transition regime," *Int. J. Heat Mass Transf.*, vol. 43, no. 1, pp. 127–138, 2000, doi: 10.1016/S0017-9310(99)00113-1.

[61] P. A. Bejarano and Y. A. Levendis, "Single-coal-particle combustion in O2/N2 and O2/CO2 environments," *Combust. Flame*, vol. 153, no. 1–2, pp. 270–287, 2008, doi: 10.1016/j.combustflame.2007.10.022.

[62] J. L. Gottfried, "Laser-induced plasma chemistry of the explosive RDX with various metallic nanoparticles," *Appl. Opt.*, vol. 51, no. 7, pp. 13–21, 2012, doi: 10.1364/AO.51.000B13.

[63] S. M. Richardson, "Fluid mechanics.," pp. 159–160, 1989.

Appendix 1: MATLAB code for solving Signal Equation

```
% This LaTeX was auto-generated from MATLAB code.
% To make changes, update the MATLAB code and export to LaTeX again.
\documentclass{article}
\usepackage[utf8]{inputenc}
\usepackage[T1]{fontenc}
\usepackage{lmodern}
\usepackage{graphicx}
\usepackage{color}
\usepackage{hyperref}
\usepackage{amsmath}
\usepackage{amsfonts}
\usepackage{epstopdf}
\usepackage[table]{xcolor}
\usepackage{matlab}
\sloppy
\epstopdfsetup{outdir=./}
\graphicspath{ {./SignalEquationSolv_images/} }
\begin{document}
\begin{matlabcode}
% Define the Signal Equation
syms c2 Ep1 Ep2 El1 El2 ramda1 ramda2 TL
Tp=c2*((1/ramda2)-(1/ramda1))*(c2*((1/ramda2)-
(1/ramda1))*1/TL+log((Ep1/Ep2)*((ramda1/ramda2)^1.2)*(El2/El1)))^-1
\end{matlabcode}
\begin{matlabsymbolicoutput}
Tp =
\hskip1em $\displaystyle -\frac{c_2 \,{\left(\frac{1}{{\textrm{ramda}}_1 }-
\frac{1}{{\textrm{ramda}}_2 }\right)}}{\log \left(\frac{{\textrm{El}}_2
\,{\textrm{Ep}}_1
\,{{\left(\frac{{\textrm{ramda}}_1 }{{\textrm{ramda}}_2 }\right)}}^{6/5} }{{\textrm{El}}
_1 \,{\textrm{Ep}}_2 }\right)-\frac{c_2 \,{\left(\frac{1}{{\textrm{ramda}}_1 }-
\frac{1}{{\textrm{ramda}}_2 }\right)}}{\textrm{TL}}}$
\end{matlabsymbolicoutput}
\begin{matlabcode}
% Path to the data file
filePath = 'Path to the file';
data = xlsread(filePath);
```

```
Ep1_values = data(:, 1); % Modify based on location of Ep1 column in excel file
Ep2_values = data(:, 2); % Modify based on location of Ep2 column in excel file
% Calculate and output Tp for each data through loop
for i = 1:size(data, 1)
    Tp_i = subs(Tp, [c2, Ep1, Ep2, El1, El2, ramda1, ramda2, TL],
[1.438776877*(10^-2), Ep1_values(i), Ep2_values(i), 2.62, 1.48, 998*10^-9,
810*10^-9, 2392]);% Substitute each value
    % Handling when Tp_i value is NaN or infinity
    if isnan(Tp_i) || isinf(Tp_i)
        disp(['Tp_', num2str(i), ': Undefined or infinite']);
    else
        % Convert to string using char function instead of num2str
        disp([char(vpa(Tp_i))]);
    end
end
\end{matlabcode}
\begin{matlaboutput}
1593.059111541605144693174704697 6
1803.597003745996692556213395194 9
1832.067621195356716113525491154 4
2016.869808787334995851912596877 4
2038.316990056787390151080699538 7
2064.030351656105018458938708963 8
2078.933169095388843946383273847 2
2174.198167804677676568685207518
2213.671949481849650332027222426 1
2208.507297637997435570884910730 1
2230.230014969309183294570854286 1
2216.982994268907011700157906928 8
2185.195997926412221313504161892 4
2186.235945312801097152619333987 5
2067.982553627946994736035251657 5
2115.259284664719009574032232404 7
2050.233703708360815737629113744 2
1942.500204961259084607092354182 2
1909.690878965957873823875347541 7
1878.494533257782084352317912013 5
1894.168336784391562726043789220 1
1938.332353186182335257210030257
1926.234420517784299468509875641 4
1965.294586351453725518846310541 9
2005.689973058607119185383845086 3
2027.873697815631301414190479721 7
2077.999285785674709960654135971
2091.988367976583498624518618423
```

2101.266116117006757543665035930 4
2101.932303298640098526452875448 7
2109.027466227603251850462320488 7
2113.594003573040902837620468933 2
2121.210946788934923202018324280 3
2142.743575521458466733131226813
2153.656633036327013720445965108 2
2148.885690966973849814955995542
2123.238302969230221988350173899 9
2096.654003829170863152602446080 1
2081.770416146510561415583233593 5
2090.777717639125758585993503558 8
2102.289360907139462368272506533
2033.466508127870022868194302689 1
\end{matlaboutput}
\begin{matlabcode}
\end{matlabcode}
\end{document}

Appendix 2: MATLAB code for solving $\frac{dT_p}{dt}$

dTp/dt Calculation

```
% This LaTeX was auto-generated from MATLAB code.
% To make changes, update the MATLAB code and export to LaTeX again.
\documentclass{article}
\usepackage[utf8]{inputenc}
\usepackage[T1]{fontenc}
\usepackage{lmodern}
\usepackage{graphicx}
\usepackage{color}
\usepackage{hyperref}
\usepackage{amsmath}
\usepackage{amsfonts}
\usepackage{epstopdf}
\usepackage[table]{xcolor}
\usepackage{matlab}
\sloppy
\epstopdfsetup{outdir=./}
\graphicspath{ {./dTdtCalculation_images/} }
\begin{document}
\begin{matlabcode}
syms alpha dp pa kb Ta gamma Tp ma ro cp
dTdt=(3*alpha*pa*((8*kb*Ta)^0.5)*(gamma+1)*(1-
Tp/Ta))/(4*((pi*ma)^0.5)*(gamma-1)*ro*cp*dp)
\end{matlabcode}
\begin{matlabsymbolicoutput}
dTdt =
\hskip1em $\displaystyle -\frac{3\,\alpha \,\textrm{pa}\,{\left(\gamma
+1\right)}\,{\left(\frac{\textrm{Tp}}{\textrm{Ta}}-
1\right)}\,\sqrt{8\,\textrm{Ta}\,\textrm{kb}}}{4\,\textrm{cp}\,\textrm{dp}\,\textrm{ro}\,\
sqrt{\pi \,\textrm{ma}}\,{\left(\gamma -1\right)}}$
\end{matlabsymbolicoutput}
\begin{matlabcode}
alpha_val=0.03
\end{matlabcode}
\begin{matlaboutput}
alpha_val = 0.0300
\end{matlaboutput}
\begin{matlabcode}
dp_val=50*10^-6
\end{matlabcode}
```

\begin{matlaboutput}
dp_val = 5.0000e-05
\end{matlaboutput}
\begin{matlabcode}
pa_val=101325
\end{matlabcode}
\begin{matlaboutput}
pa_val = 101325
\end{matlaboutput}
\begin{matlabcode}
kb_val=8.314;
Ta_val=1400
\end{matlabcode}
\begin{matlaboutput}
Ta_val = 1400
\end{matlaboutput}
\begin{matlabcode}
gamma_val=1.4
\end{matlabcode}
\begin{matlaboutput}
gamma_val = 1.4000
\end{matlaboutput}
\begin{matlabcode}
ma_val=0.0304
\end{matlabcode}
\begin{matlaboutput}
ma_val = 0.0304
\end{matlaboutput}
\begin{matlabcode}
ro_val=1.18*10^3
\end{matlabcode}
\begin{matlaboutput}
ro_val = 1180
\end{matlaboutput}
\begin{matlabcode}
cp_val=1380
\end{matlabcode}
\begin{matlaboutput}
cp_val = 1380
\end{matlaboutput}
\begin{matlabcode}
excelFilePath = '/Users/hayoungj/Library/Mobile
Documents/com~apple~CloudDocs/Fall
2022/3P/ResearchData/THESISDATA/Excel4.xlsx';
data = xlsread(excelFilePath, 'Sheet3');

```
Tp_values = data(:, 2);
for i = 1:size(data, 1)
    dTdt_i = subs(dTdt, [alpha, dp, pa, kb, Ta, gamma, ma, ro, cp, Tp], [alpha_val,
dp_val, pa_val, kb_val, Ta_val, gamma_val, ma_val, ro_val, cp_val,
Tp_values(i)]);
    disp([char(vpa(dTdt_i))]);
    if isnan(dTdt_i) || isinf(dTdt_i)
        disp(['dTdt_', num2str(i), ': Undefined or infinite']);
    end
end
\end{matlabcode}
\begin{matlaboutput}
-98376.636662675003686368065672775
-96806.954383294405745295495006716
-93040.410493770576517326526096246
-77048.292234902128189395531565539
-64282.601918303429802720805061557
-60394.918885420991379269617306811
-56698.363097745302138849956447426
\end{matlaboutput}
\end{document}
```